Modelling magnetic fields and plasma flows in the magnetosphere of Jupiter

D. Millas[1,*], N. Achilleos[1], P. Guio[b], C. S. Arridge[c]

[a]*Department of Physics and Astronomy, University College London, Gower Street, London WC1E 6BT, UK*
[b]*Department of Physics and Technology, Arctic University of Norway, Tromsø, Norway*
[c]*Department of Physics, Lancaster University, Bailrigg, Lancaster, LA1 4YB, UK*

Abstract

The magnetic fields of the giant planets, Jupiter and Saturn, deviate significantly from a pure magnetic dipole and the cold plasma is mostly centrifugally confined near the equator. The additional contribution of the azimuthal currents leads to the stretching of the magnetic field and the formation of a characteristic, disc-type structure known as a magnetodisc. We present here an updated version of a numerical implementation of Caudal's iterative scheme, used to create models of the magnetosphere. In particular, we include newer equatorial density, temperature and hot plasma profiles obtained from Galileo data. Finally, we describe and use an algorithm to update the angular velocity profile after the end of the iterative process, using information from the magnetodisc. We also present comparisons between the azimuthal current and plasma flow predicted by our model and those derived from spacecraft observations.

Keywords: planetary magnetic fields, angular velocity,
magnetohydrodynamics (MHD), numerical methods

---

1. Introduction

The region of influence of a planetary magnetic field, commonly known as the planetary magnetosphere, is a dynamic structure affected by both external

---

[*] Corresponding author
Email address: `dimitrios.millas@ucl.ac.uk` (D. Millas)

Preprint submitted to Planetary and Space Science *November 25, 2022*

and internal drivers. To model the morphology of the magnetosphere, we first need to describe the planetary magnetic field with sufficient accuracy. A good approximation of the global, large scale magnetic field for the Earth may be obtained via a simple magnetic dipole, with a tilt between the magnetic and the rotation axis of $\sim 11.5^o$. However, observations have shown that the magnetic fields of the giant planets Jupiter and Saturn are much more complex.

The magnetosphere of Jupiter is a quite unique entity in our Solar System. It can extend up to $\simeq 100R_J$ (Jovian radii) on the dayside in quiet solar conditions, while an average value for the magnetopause location being $\sim 75R_J$. Its (equatorial) magnetic field magnitude (due to the internal dynamo) is close to $4 \cdot 10^5$ nT and it is rotating remarkably fast, with a period of slightly less than 10 hours. Another important element is the presence of the volcanic moon Io, which acts as the main source of plasma in the magnetosphere. A similar situation is observed at Saturn, where the plasma source is the icy moon Enceladus. The solar wind, in contrast with the terrestrial case, is a minor contributor to the plasma content of the magnetosphere.

A striking difference between the magnetosphere of the Earth and the magnetospheres of Jupiter and Saturn is the presence of a strong equatorial current sheet and a plasma disc, which modifies the magnetic field profile to a structure known as a *magnetodisc*. The deviation of the magnetic field from a dipole becomes evident as the equatorial distance from the planet increases (see Fig. 1 for a schematic representation of the Jovian magnetosphere and also Fig. 24.1 from Khurana et al. (2004) for a more general case). The transition between the two different profiles is observed between the inner magnetosphere (equatorial distances up to $10R_J$, where the magnetic field is close to a dipole, and in the middle magnetosphere $(10 - 40R_J)$, where the stretching of the magnetic field lines is clearly visible.

Both giant planets are rapid rotators and the resulting source of energy and angular momentum is a key driver of their magnetosphere. The magnetodisc was proposed by Gledhill (1967) as a consequence of the centrifugal force that acts on plasma and favours its accumulation close to the equator. This

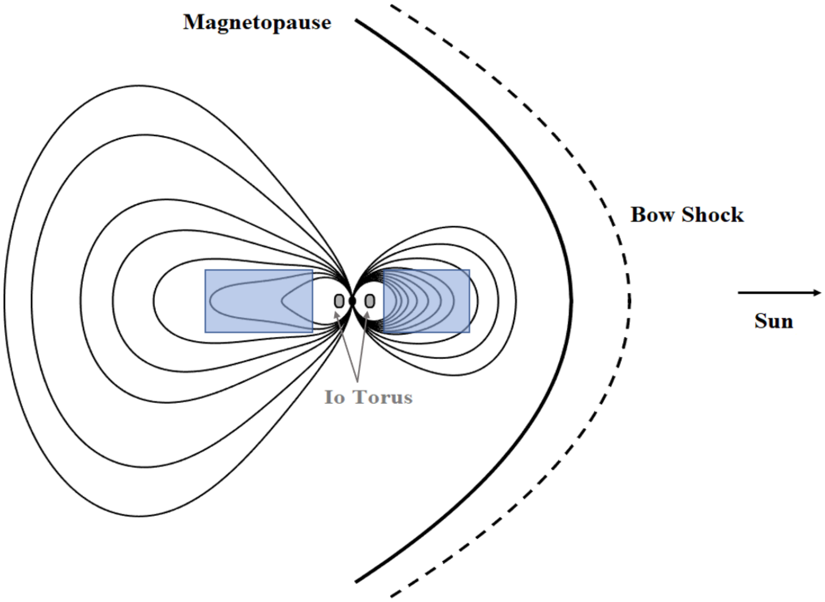

Figure 1: A simple sketch of a meridian cut of the dayside and nightside Jovian magnetosphere (not to scale), assuming a spin-aligned planetary magnetic field. The volcanic moon Io is located at a distance of roughly $6R_J$, with the ejected material forming the characteristic torus. The magnetic field lines resemble a magnetic dipole near the planet, but in the middle magnetosphere (equatorial distances $10-40R_J$, show the characteristic elongated shape that defines the magnetodisc. For the more general case of a misaligned magnetic field, see the sketch in Fig. 24.1 from Khurana et al. (2004).

structure, in the case of Jupiter, was later confirmed by various missions, e.g. Pioneer 10 (Simpson et al., 1974; Hill et al., 1974; Smith et al., 1975), Voyager 1 (Connerney et al., 1982) and Galileo Orbiter (Kivelson et al., 1997b).

The associated current sheet and its effects on the magnetospheres of Jupiter and Saturn were examined in Connerney et al. (1981b,a, 1983). Later, a combination of magnetohydrodynamics (MHD) equilibrium and observations was used by Caudal (1986) in order to construct a self-consistent model of the Jovian magnetosphere based on the balance between centrifugal, magnetic and plasma pressure forces. The presence of a hot plasma is important as it provides an additional pressure term in the force balance, with implications on the size of the magnetosphere.

Caudal's model was extended and implemented in a numerical code (UCL/AGA) able to calculate the magnetic field profile, using appropriate parameters for the Jovian or Kronian magnetosphere by Achilleos et al. (2010). These models assumed time independence (stationary magnetosphere); however, temporal variability was evident in Voyager or Galileo data and was also recently shown by Huscher et al. (2021) using Juno data. In particular, examination of the plasma density from Juno data between 15-50R_J revealed small scale structures with typical size $< 1R_J$ and temporal variability in the scale of minutes. Small scale structures in the magnetic field were also reported by Kivelson et al. (1997a) and interchange structures by Thorne et al. (1997). All these scales can be ignored as a first approximation, since we examine the large scale structure of the magnetosphere.

The availability of data from more recent space missions led to an update of the above profiles regarding the current sheet (Khurana, 2001; Connerney et al., 2020; Lorch et al., 2020), the plasma properties (density, temperature) on the equator (Bagenal and Delamere, 2011; Bagenal et al., 2016) and the presence of energetic particles (Mauk et al., 2004; Huscher et al., 2021). We have implemented the new equatorial profiles in the UCL/AGA code, which now includes initial conditions appropriate for the Voyager and Galileo eras. The model can, in principle, be further developed to make use of plasma moments from the Juno mission in the upcoming future.

An important element in the model is the angular velocity of the plasma, which also quantifies the centrifugal force. The magnetospheric plasma near Jupiter is approximately corotating with the planet; at distances larger than the orbit of Io ($\sim 6R_J$), the plasma shows a significant sub-corotation. For a magnetic dipole, magnetohydrodynamics and angular momentum conservation dictate a specific profile for the angular velocity with equatorial distance (Hill, 1979). Since the magnetic field of giant planets is significantly modified due to the magnetodisc, the angular velocity is, also modified compared to the "pure dipole" case (Pontius, 1997). The issue of the angular velocity in the magnetospheres of giant planets has been examined by various authors since Hill's initial study. Here we will review the key elements of Hill (1979) and Pontius (1997); we also note that Nichols and Cowley (2003, 2004) investigated Pontius' method for different formulations of ionospheric conductivity.

In this work, we introduce an updated numerical adaptation of Caudal's iterative scheme which can be used to produce models of the Jovian magnetosphere. These models reproduce quite accurately the large scale structure of the magnetosphere and their predictions can be compared with angular velocity data and equatorial current profiles from empirical models. A secondary part of the work is the numerical investigation of the algorithms used to update the angular velocity.

The paper is structured as follows: in Section 2 we describe the method used to construct the global magnetosphere including a magnetodisc; in Section 3 we describe the implementation of new Galileo data in the equatorial initial conditions. These include density, temperature and hot plasma content profiles, inferred from in situ observations plus a new algorithm to treat the plasma angular velocity in a consistent way. In Section 5 we compare the output from the magnetodisc model with observations of the plasma angular velocity and models for the azimuthal current. Numerical tests are provided in an appendix.

2. Caudal's magnetodisc model

First, we will give a brief overview of Caudal's original model and discuss the key equations, as presented in (Caudal, 1986). Then, we will present the numerical implementation of the model in the UCL/AGA magnetodisc code by (Achilleos et al., 2010). For a more detailed description of the model and the code, we refer the reader to these two articles.

2.1. Basic equations

Caudal examined a stationary, axisymmetric magnetosphere (imposing axial symmetry about the rotation/magnetic axis with ϕ denoting the azimuthal direction in spherical or cylindrical coordinates). The spin-aligned dipole assumption is justified due to the small dipole tilt ($\sim 10^o$) with respect to the rotation axis. The small angle approximation was also justified in the analysis of Cummings et al. (1980). Phipps and Bagenal (2021) explored the tilt of the centrifugal equator due to the influence of the current sheet. The displacement of the centrifugal equator (towards the magnetic equator) is expected to be small up to distances of $30R_J$ and is therefore ignored in our study. We mention here again that we ignore any temporal or spatial fluctuation e.g. in the density, as these are typically small in size $< 1R_J$ or very short (few minutes). It is also implied in the model that there is sufficient time to connect the magnetodisc to the planet via currents.

Assuming a force balance in both (cylindrical) radial and meridional directions between the magnetic force, the pressure gradient and the centrifugal force:

$$\mathbf{J} \times \mathbf{B} - \nabla P + n_i m_i \rho \omega^2 \hat{\boldsymbol{\rho}} = 0 \tag{1}$$

In the above expression, $\mathbf{J}, \mathbf{B}$ are the current density and the magnetic field respectively, P is the total thermal plasma pressure, n_i is the ion number density, m_i the mean ion mass, ρ is the cylindrical distance from the rotation axis, $\hat{\boldsymbol{\rho}}$ is the cylindrical radial unit vector, ω the angular velocity of the plasma. The contribution of the gravitational force beyond a few Jovian radii is minimal and can be safely neglected. In addition, Caudal's model assumes isotropic plasma; this effectively ignores the anisotropy force contribution; this, however, is significant in the middle magnetosphere (Nichols et al., 2015).

Using the $\nabla \cdot \mathbf{B} = 0$ condition, Caudal expressed the magnetic field via the cross product of two "Euler potentials" Stern (1970):

$$\mathbf{B} = \nabla\alpha \times \nabla\beta_E \quad , \tag{2}$$

where the scalar functions α and β_E are the Euler potentials (using the subscript $_E$ to avoid confusion with the plasma β), in general functions of r, θ, ϕ in spherical coordinates. Exploiting the axisymmetry of the system, the Euler potentials can be simplified and be rewritten as follows:

$$\alpha = \alpha(r,\theta) \quad , \tag{3}$$

$$\beta_E = R_p\phi \quad . \tag{4}$$

where R_p is the radius of the planet. If we examine a meridional cut of the magnetosphere, then β_E is a constant and can be omitted from the rest of the analysis. The magnetic field, again in spherical coordinates, can thus be expressed via α only:

$$B_r = \frac{1}{r^2 sin\theta}\frac{\partial\alpha}{\partial\theta} \tag{5}$$

$$B_\theta = -\frac{1}{r sin\theta}\frac{\partial\alpha}{\partial r} \tag{6}$$

where we also used the definition of the azimuthal current $\mathbf{J}_\phi = \frac{1}{\mu_o}\nabla \times \mathbf{B}$, which is a function of α as well.

Caudal showed that the total plasma pressure (calculated from the cold and hot plasma populations) and the centrifugal force can also be expressed via α. Consequently, the original problem of force equilibrium is then reduced to the calculation of the Euler potential α only, which is in turn obtained by solving the following differential equation (now in normalized units):

$$\frac{\partial^2\alpha}{\partial r^2} + \frac{1-\mu^2}{r^2}\frac{\partial^2\alpha}{\partial\mu^2} = -g(r,\mu,\alpha) \quad , \tag{7}$$

where r is the radial distance in spherical coordinates, μ replaces the colatitude θ ($\mu = \cos\theta$) and g is the source function defined by the plasma pressure and its angular velocity. This expression is physically equivalent to equation 1, replacing all terms with alternative expressions involving α; it basically incorporates all the mechanical forces (centrifugal, pressure gradients) acting on the plasma. The source function can be used to calculate the azimuthal current J_ϕ, which is a key element for the stretching of the field lines near the equator.

In the original method proposed by Caudal, the physical parameters along the equator (e.g. density, temperature) were constrained from observations and specifically, data from Voyager 1 (Bagenal and Sullivan, 1981) (although a correction was given later in Bagenal et al. (1985)). In addition, a hot plasma population (plasma with thermal ion energy significantly higher than their rotational kinetic energy) is added in the system, contributing to the total thermal plasma pressure P. The distribution function of the hot plasma was examined by Krimigis et al. (1981) using Voyager 1 and 2 data and it was reported that the hot ions dominate the plasma pressure. The hot plasma content is modelled via the product of the equatorial hot plasma pressure (P_h) and the flux tube volume (V_h), defining the hot plasma index:

$$K_h = P_h V_h \qquad . \tag{8}$$

Up to $\sim 8R_J$, the K_h index is assumed to be constant with radial distance.

The equatorial angular velocity as a function of the equatorial distance is obtained from Hill's theory (Hill, 1979), using the conservation of angular momentum and magnetic flux. Hill initially assumed that the viscosity of the atmosphere is large enough to transport the planetary angular momentum to the ionosphere. The rate of transport itself depends on the ionospheric conductivity, which must also be sufficiently large to enforce corotation of the magnetospheric plasma. However, beyond a critical radius the magnetic field may be too weak to maintain the plasma in corotation; in addition, outward transport or sources of plasma can limit corotation as well. An approximate distance where the corotation breaks down can be calculated (also for Jupiter) using the height integrated-conductivity and the outward plasma flux. Hill's theory provides an approximate solution for the profile of the angular velocity ω based on a magnetic dipole field. We will discuss in more detail the angular velocity treatment in a following section.

2.2. Iterative process for the Euler potential α

Up to this point, all physical variables are expressed via the Euler potential α and the equatorial parameters (ion density n_i, temperature T, angular velocity ω) are inferred from observations. The final step in Caudal's method is to numerically solve equation 7 using an expansion of α in terms of Jacobi polynomials (to satisfy the homogeneous part of the differential equation) via an iterative process. As an initial condition, the magnetic field is assumed to be a dipole, described using the previous notation as:

$$\alpha_{init} \equiv \alpha_{dip} = \frac{1-\mu^2}{r} \tag{9}$$

After every iteration, we calculate a "perturbed" magnetic field and the associated source function g before proceeding to the next iteration. This process provides a more accurate description of the magnetic field, capturing the dipole-like behaviour at the near-planet regions and the magnetodisc structure at larger equatorial distances. The iterative process for the calculation of α includes an intermediate step, where we calculate a linear combination of the "new" and the "old" solution, before proceeding to the next iteration:

$$\alpha = \nu_{i-1}\ \alpha_{i-1} + \nu_i\ \alpha_i \quad , \tag{10}$$

where α is the initial value for the next iteration, ν_i, ν_{i-1} are the fractions of the "old", mixed solution α_{i-1} and the "pure" α_i solution respectively. In principle, any combination of ν_i, ν_{i-1} in the interval [0,1] can be used (restricted only by the requirement $\nu_i + \nu_{i-1} = 1$). Caudal used an equal contribution from the two solutions (thus $\nu_i = 0.5 = \nu_{i-1}$) before the next iteration. This "mixing" of the solutions stabilizes the convergence towards the final solution. The iterative process stops when the relative difference $(\alpha_i - \alpha_{i-1})/\alpha_i$ becomes smaller than a user-defined threshold. This threshold is not entirely independent of the mixing factors $\nu_{i,i-1}$, as shown below.

A suitable convergence criterion for the calculation of the Euler potential α can be defined as:

$$|(\alpha - \alpha_{i-1})/\alpha_{i-1}| = \nu_i |(\alpha_{i-1} - \alpha_i)/\alpha_{i-1}| < \delta \tag{11}$$

where δ is a prescribed convergence parameter, typically a number $\sim 10^{-3}$ and is set as the threshold mentioned above. Rearranging the inequality terms, we find:

$$|(\alpha_i - \alpha_{i-1})/\alpha_{i-1}| < \delta/\nu_i \tag{12}$$

This means that the pure solution from Caudal's scheme and the value used for the most recent iteration differ relatively no more than δ/ν. This fraction determines the final level of convergence. Different values of ν can be used depending on the actual system and the stability of the process (which is a form of numerical "relaxation"). Models with significant contribution from the hot plasma population usually require smaller steps in the process, which translate into smaller values of ν_i. This requires an adjustment of the convergence parameter accordingly to maintain the same δ/ν_i. In the cases presented in this paper, we set the ratio δ/ν_i to 10^{-2} and as such, the convergence parameter is always $\delta \leq 5 \cdot 10^{-3}$.

A typical example of a magnetodisc field, obtained from the numerical implementation of Caudal's method, is shown in Fig. 2, via the magnetic potential α. The dipole approximation is valid near the planet; however, the difference becomes prominent at larger distances. For comparison, see the solution (via the magnetic field lines) in Figure 6 from (Caudal, 1986).

To justify the connection between the planet and the magnetodisc, we performed the following simple calculations. Using a typical magnetodisc model with $R_{mp} = 80R_J$ and $K_h = 3{\cdot}10^7$ Pa m T^{-1}, we found that $\sim$ 80% of the mass in a flux tube is confined to latitudes $< 6^o$ at a distance of $\sim 40R_J$. The Alfvén travel time in that case is ~3.1h. Repeating the calculations for larger distances ($70R_J$), we found that 80% of the mass is now confined to latitudes $< 30^o$ and

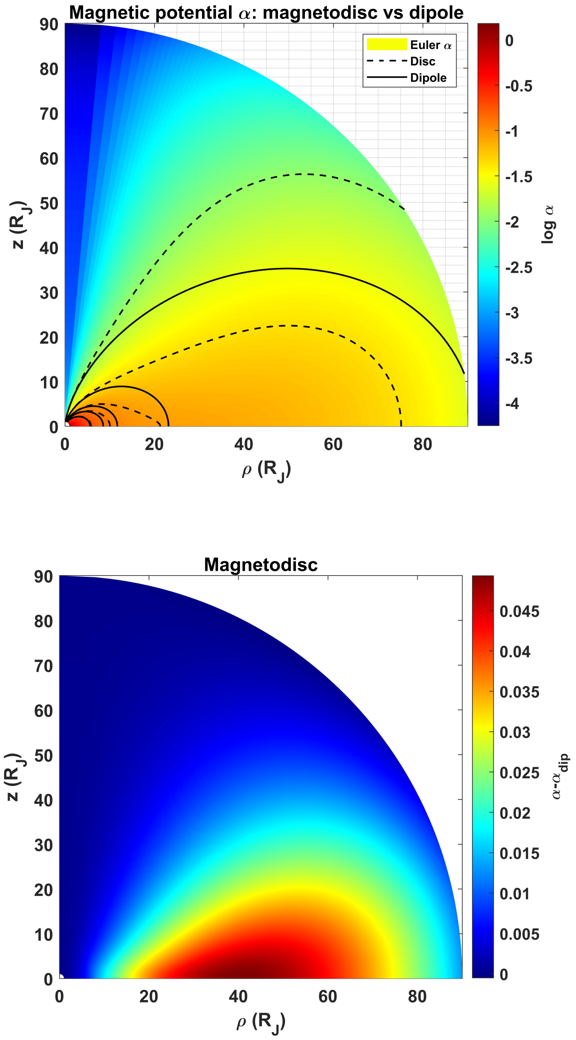

Figure 2: Typical example of a magnetodisc using Caudal's theory. **Top:** the magnetic potential α (in colour, log scale, dimensionless) in the northern hemisphere ($\theta = 0{-}90$ degrees), the total magnetic potential (solid contours) and the magnetic dipole (dashed contours). Isocontours of α are equivalent to shells of magnetic field lines. The contours overlap near the planet but differ as we examine larger radii. **Bottom:** Magnetic (Euler) potential α , removing the contribution from the dipole, visualising the magnetodisc.

the Alfvén travel time is ~ 7.6h. In both cases there is most likely sufficient time for the magnetodisc to communicate with the inner boundary. Since the bulk of the mass is confined near the equator (even for large equatorial distances), the Alfvén velocity is only reduced at this region. In Delamere and Bagenal (2010), the "lifetime" (loss of plasma) is less than 1 day, which should be enough to preserve the connection.

3. Additions in the UCL/AGA code: Equatorial conditions

As we mentioned in the previous section, Caudal originally used data from Voyager 1 to set the equatorial plasma conditions (temperature, density and flux tube content) and the hot plasma pressure via the K_h index. We will now present the incorporation of newer data for the equatorial plasma conditions and hot plasma pressure in our numerical implementation of Caudal's model. We note that Nichols et al. (2015) also produced models of the magnetodisc using Galileo input.

The first element is the use of Galileo data, obtained from the empirical fits of (Bagenal and Delamere, 2011; Bagenal et al., 2016), in order to determine the initial conditions on the equator (temperature, density and flux tube content). Then, the hot plasma pressure is introduced in tabulated form, using the data from (Mauk et al., 1996, 2004). The final element is the introduction of an angular velocity updating algorithm according to the model of (Pontius, 1997), using the full magnetodisc field.

3.1. Equatorial plasma conditions and flux tube content

We begin by giving an overview of the equatorial plasma parameters, as presented in detail by (Bagenal and Delamere, 2011) and (Bagenal et al., 2016). Using data from the Plasma Science Instrument (PLS) of Galileo, the authors provided estimates for the number density of the equatorial plasma (n in cm^{-3}), its temperature (T in eV) and the flux tube content (NL^2 in ions/Wb).

Their empirical fit of the data for the equatorial distribution of the electron density was:

$$n_{eq}(\rho) = 1987\ (\rho/6)^{-8.2} + 14\ (\rho/6)^{-3.2} + 0.05\ (\rho/6)^{-0.65} \qquad , \qquad (13)$$

where ρ is again the equatorial distance expressed in Jovian radii. This expression can also be used for the ions, assuming their charge state. However, this fit is not valid for radii smaller than approximately 6 Jovian radii (see figure 9 in (Bagenal et al., 2016)). To amend this, we replace this fit with a piecewise function:

$$n_{eq}(\rho) = 1987\ (\rho/6)^{-8.2} + 14\ (\rho/6)^{-3.2} + 0.05\ (\rho/6)^{-0.65} \qquad , \quad \rho \geq 6, \quad (14)$$

$$n_{eq}(\rho) = n\big|_{\rho=6}\ (\rho/6)^{8} \qquad , \qquad \rho < 6. \quad (15)$$

Although the part of the density profile for small distances does not originate from actual observations, it is continuous at $\rho = 6$ and satisfies the physical requirement of a rapid decrease in density inside the orbit of Io.

For vertical distances close to the equator, assuming a single species plasma, the number density at a height z from the centrifugal (the rotational) equator can be approximated with an exponential decrease, as suggested by (Hill and Michel, 1976) for a magnetic dipole aligned with the rotational axis:

$$n(\rho, z) = n(\rho, z)\big|_{z=0}\ e^{-(z/H)^2} \qquad (16)$$

where H is the scale height, defined via the temperature and the angular velocity:

$$H = \sqrt{\frac{2kT}{3m\omega^2}} \qquad . \qquad (17)$$

An empirical fit for the scale height is given again by Bagenal and Delamere (2011) (using plasma sheet crossings), which can then be used to calculate the equatorial temperature distribution as well.

The fits for the scale height and the temperature presented above reproduce quite well the data for distances between 6 and 30 Jovian radii (see once more figure 9 in (Bagenal et al., 2016)). However, as seen in the density, the fit is not valid for small distances (up to 6 Jovian radii). To amend this, we modified the profiles using now a linear increase in temperature in the interval $[1, 6)R_J$ (in tandem with the sharp increase in the equatorial density shown before), in the same distance range. The scale height for small distances can be calculated from the linear temperature profile using Eq. 17. The final temperature, density and scale height profiles are always continuous at $r = 6R_J$. The Galileo instruments were able to detect higher energies, leading to higher temperatures, as shown in Fig. 3.See also Figure 4 from Nichols et al. (2015), showing a similar profile for the cold plasma temperatures, used in their own magnetodisc code.

Finally, we also need to specify the flux tube content (i.e. the total amount of ions in a flux shell or the number of ions per unit magnetic flux). Since the initial magnetic field profile is assumed to be a dipole, we may use the formula of Siscoe (1978) as a meaningful approximation. According to Siscoe (1978); Bagenal et al. (2016), this can be expressed as follows:

$$NL^2 = 2\pi R_J^2 L^3 \int n \frac{B_J}{B} ds \tag{18}$$

$$\simeq 4 \cdot 10^{30}\ L^3\ n\big|_{z=0}\ H \tag{19}$$

where L is the equatorial crossing distance in Jovian radii (R_J), B_J is the equatorial magnetic field of Jupiter and ds is the line element along a magnetic field line.

3.2. Hot plasma pressure

Using Energetic Particle Detector (EPD) data from Galileo, Mauk et al. (1996, 2004) provided hot plasma spectra and velocity moments for various energetic ions (H, He, O, S). The suggested profiles were obtained for distances from 6 to $46R_J$, near the equatorial plane and covered ion energies from 50 keV to roughly 50 MeV (depending on the equatorial distance and the ion species).

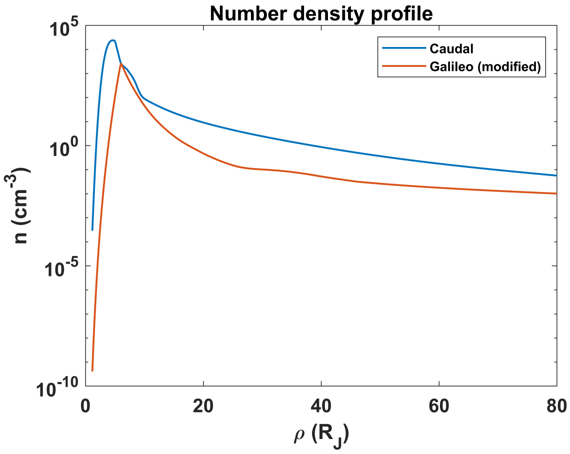

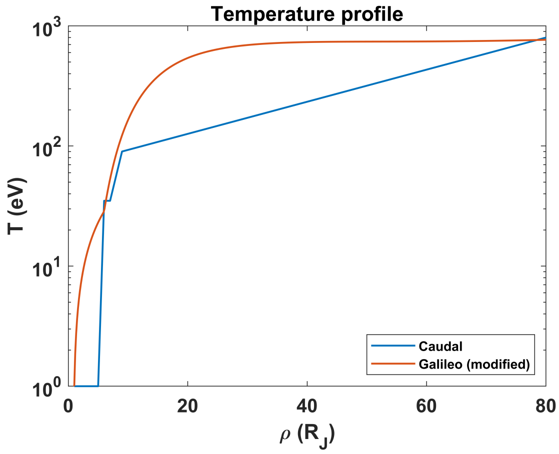

Figure 3: **Top:** Comparison between the equatorial density profiles provided by Caudal Caudal (1986) and Bagenal et al. (2016) (modified for small distances). **Bottom:** The temperature profile provided by Caudal for the cold plasma (a linear piecewise function) and the smooth, continuous profile obtained from the modified Galileo fits. The higher temperatures obtained using Galileo data are due to the fact that Galileo could measure higher energies. See also Figure 4 from Nichols et al. (2015).

As mentioned in Section 2.1, the hot plasma pressure is parametrized via the hot plasma index K_h, the product of the hot plasma pressure P_h and the flux tube volume V_h. For the Voyager conditions, we usually assume values of $K_h \sim 1 - 3 \cdot 10^7$ Pa m T^{-1} (temperature of hot plasma given by Krimigis et al. (1981) and used by Caudal (1986) as an input for his iterative method). In contrast with the previous initial conditions, here it is necessary to use an appropriate value for the flux tube volume, consistent with the magnetodisc structure (rather than a dipole approximation). This is obtained numerically from a typical magnetodisc model where, as a first approximation, we used the initial conditions suggested by Caudal. If the hot plasma index in a Caudal-type model is of the order of $2 \cdot 10^7$ Pa m T^{-1}, then the model represents well an average state of the Jovian magnetosphere and thus the approximation in the flux tube volume is sufficient (Caudal, 1986). The difference between the flux tube content and the hot plasma pressure using Galileo and Voyager data is shown in Fig. 4. For the original hot plasma pressure profile from EPD data, we refer the reader to figure 4 of (Mauk et al., 2004).

A comparison between the cold and hot equatorial plasma pressure for the Voyager and Galileo "eras" is shown in Fig. 5. The dependence of the hot plasma pressure on the K_h index for the Galileo profiles is treated as a vertical shift of the whole pressure profile, according to the ratio K_h/K_{ho}, where $K_{ho} = 3.5 \cdot 10^7$ Pa m T^{-1}, obtained from the implementation of hot plasma pressure from (Mauk et al., 2004) as explained above.

Using either Voyager or Galileo conditions, the maximum value of plasma β in our runs is approximately $\beta \simeq 12$, with the hot plasma contributing significantly more, in agreement with (Achilleos et al., 2010). Moreover, the hot plasma beta β_h is larger than the cold plasma beta. This is consistent with the hot plasma pressure dominating the plasma pressure (Krimigis et al., 1981) and this is not affected when we consider the higher cold plasma beta values reported by Frank and Paterson (2002 and Frank et al. (2002) found specifically on the G07 and G08 orbits (studying thermal plasmas in the magnetotail). The values of plasma β indicate that the plasma pressure has a significant contribution to

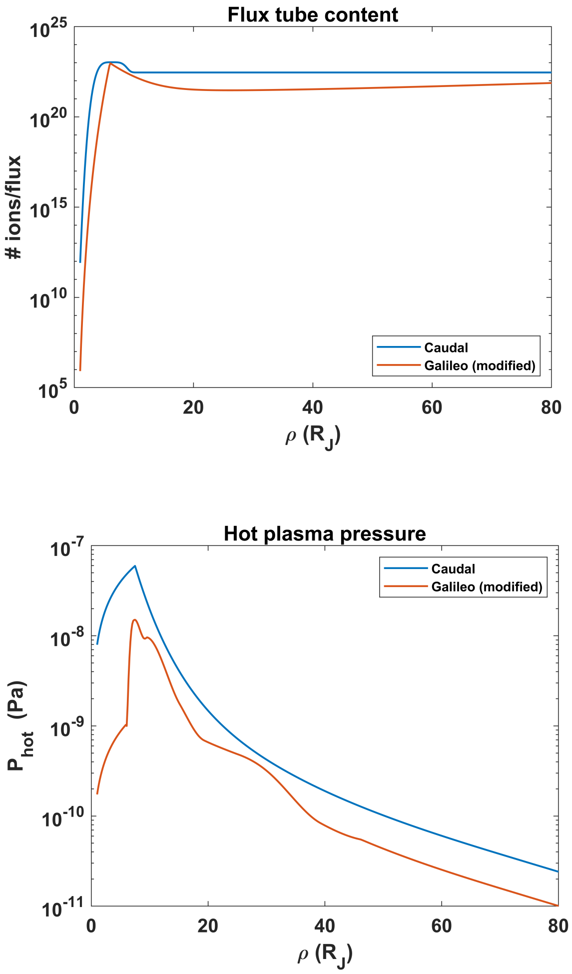

Figure 4: **Top:** Flux tube content comparison between Caudal's model and the obtained profile from the modified fit of Galileo data. **Bottom:** Same for the hot plasma pressure profiles.

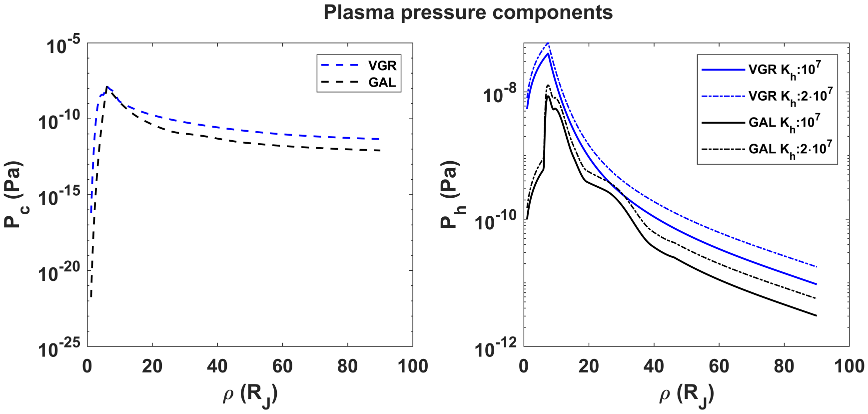

Figure 5: Pressure profiles according to Voyager (VGR) Caudal (1986) and Galileo data (GAL) Bagenal et al. (2016). **Left:** Cold plasma pressure. Its profile is independent of the value K_h and depends only on the equatorial initial conditions. **Right:** Hot plasma pressure for different K_h values. The profiles obtained from Galileo are always lower that the Voyager profiles for the same value of the hot plasma index.

the force balance.

Similar results for the equatorial number density were reported by Nichols (2011); Nichols et al. (2015), using Galileo data from Frank et al. (2002). A difference in that case is the assumption of a piecewise constant flux tube content in different regions of the magnetosphere, with a constant value for equatorial distances larger than $8R_J$. Last, we also acknowledge a report from Nichols et al. (2020) that used Juno data to derive the plasma and magnetic field conditions along the equator.

4. Additions in the UCL/AGA code: Angular velocity

In order to determine the angular velocity profile of the magnetospheric plasma, we need to calculate ω as a function of the magnetic field line equatorial crossing distance L. Then, using Ferraro's isorotation law (Ferraro, 1937) and the magnetic potential α we can obtain the angular velocity for the entire domain. We note here that the potential α is related to the integrated magnetic flux, as shown in Achilleos et al. (2010) (page 2353). The angular velocity profile, in general, cannot be obtained analytically. We will present here two methods (Hill's and Pontius') to calculate $\omega(L)$ from the equatorial magnetic field, each using a different approach. A second method to update the angular velocity, provided by Nichols and Cowley (2003); Nichols et al. (2015) is discussed in the appendix.

4.0.1. Hill's method

We will first briefly describe Hill's method (see Hill (1979) for a detailed description), an easy way to obtain an analytical solution for the angular velocity $\omega(L)$, using a simple magnetic dipole and the conservation of angular momentum and magnetic flux. This method was used by Caudal in his original magnetosphere force balance model in order to determine the angular velocity along the rotational equator (as an initial condition).

First, consider a spin-aligned dipole in spherical coordinates (r, θ, ϕ). Assume now that ions have a rotational drift velocity $\delta v = r\delta\omega \sin\theta$ (ω being the azimuthal velocity) relative to the neutral atmosphere. If we focus on a steady-state system, the net force per unit volume F_ϕ due to collisions between ions and neutral species is equal to the Lorentz force: $F_\phi = \sigma \; B_r^2 \; \delta v$, where σ is the Pedersen conductivity.

For the simple case discussed here, the torque T per unit of equatorial crossing distance L can be written as:

$$\frac{dT}{dL} = 4\pi\Sigma\delta\omega R_J^4 B_p^2 \Big(1 - 1/L^2)^{1/2}/L^3 \qquad , \tag{20}$$

where R_J is the planetary radius, B_p the equatorial magnetic field.

The angular momentum per unit equatorial crossing distance is:

$$\frac{d\mathcal{L}}{dL} = \dot{M}\omega_J R_p^2 \frac{d}{dL}[L^2(1 - \delta\omega/\omega_p)] \qquad , \tag{21}$$

where ω_J is the planetary rotation frequency and $\dot{M}$ the outward flux of plasma (in this case, due to Io).

The next step is to combine the conservation of angular momentum with equations 20, 21. In place of the angular velocity, we will introduce here the *corotation lag* f, which is the relative difference of the local angular velocity compared to the planetary rotation. To obtain the profile of the corotation lag along the equator, we must solve the following differential equation:

$$L^5 \frac{df}{dL} + \left[2L^4 + 4L_o^4 \left(1 - 1/L\right)^{1/2} \right] f - 2L^4 = 0 \qquad , \tag{22}$$

where $f = 1 - \omega/\omega_J$ is the corotation lag (ω_J the rotation velocity of Jupiter) and L is the equatorial crossing distance. The dimensionless scaling parameter L_o, depends on the planetary radius R_p, the equatorial magnetic field B_p, the total outward plasma mass flux $\dot{M}$ and the (height-integrated) Pedersen conductivity Σ_P as:

$$L_o^4 = \pi \Sigma_P R_p^2 B_p^2 / \dot{M} \qquad . \tag{23}$$

An analysis of the coupling currents between the ionosphere and the magnetosphere can be found in Cowley and Bunce (2001) (see their Figure 1 for a schematic representation). There is a connection between the Pedersen currents in the ionosphere and a $\mathbf{J} \times \mathbf{B}$ pointing opposite to the planetary rotation. These currents depend on the value of Σ_P, which is also important for L_o. Huang and Hill (1989) suggested a corrected value of Σ_P (called the effective Pedersen conductivity), which accounts for the deviation (or "slippage") of the neutral atmosphere from rigid corotation. This was later implemented by Nichols and Cowley (2003) in his angular velocity update algorithm (see Appendix A for additional information).

A solution obtained with Hill's method is shown in Fig. 6, where we present the corotation lag f and the angular velocity ω, using $L_o = 20$, which is a meaningful choice for Jupiter if we assume $\dot{M} \sim 1000$ kg/s and $\Sigma \sim 0.05 mho$. This value also produces a good agreement with the data as a function of radial distance (Hill, 1980). Analysing Hill's solution, we can identify two regions: A near corotation region (close to the planet) and the asymptotic region for large distances. In the first region, expanding up to $L \simeq 6 - 7R_J$, the magnetosphere is corotating with the planet ($f \simeq 0$); this distance is approximately equal to the orbit of Io ($\simeq 5.9R_J$). At a distance of $\simeq 11.5R_J$, we can notice the effects of the corotation lag; the angular velocity at this distance is $\simeq 0.95$ of the planetary value. For distances larger than $\simeq 70R_J$, we retrieve the asymptotic behaviour $f \simeq 1 - \pi^{1/2}\left(\frac{L_o}{L}\right)^2$ (consistent with the conservation of angular momentum). This asymptotic behaviour can be justified as follows: the magnetic field at large distances is quite weak and the system will then follow a configuration leading to the conservation of angular momentum. When the field weakens, the $\mathbf{J} \times \mathbf{B}$ force becomes far less effective at changing the angular momentum of the plasma. Thus, it tends towards a morphology where the field approaches weak values as the flow becomes closer to the case of angular momentum conservation.

4.1. Pontius's method

Following the application of Caudal's iterative method, we obtain a magnetic field morphology which includes now the magnetodisc structure. The angular velocity, however, is not anymore consistent with the new magnetic field morphology, as Hill's solution is only valid for a magnetic dipole.

We present here a method that can provide a corrected angular velocity profile using information from the magnetodisc itself (in an iterative method similar to the work of Nichols (2011)).We need to solve the "modified" Hill or Pontius' equation, as described in Pontius (1997):

$$L^5 \frac{df}{dL} + \left[2L^4 + 4L_o^4 \mu_B \cos\theta(r)\right] f - 2L^4 = 0 \qquad , \qquad (24)$$

where the difference between a more realistic magnetic field morphology (e.g. the model obtained from Caudal's method or an equivalent method producing an elongated structure) and the magnetic dipole is quantified by the term μ_B. The term $\cos\theta(r)$, called the "mapping function", connects a point on the magnetodisc - along the equator - with a footpoint on the ionosphere, following a magnetic field line of constant Euler potential α.

To solve the Pontius equation, we need first to calculate the "Pontius" term μ_B from the magnetodisc model:

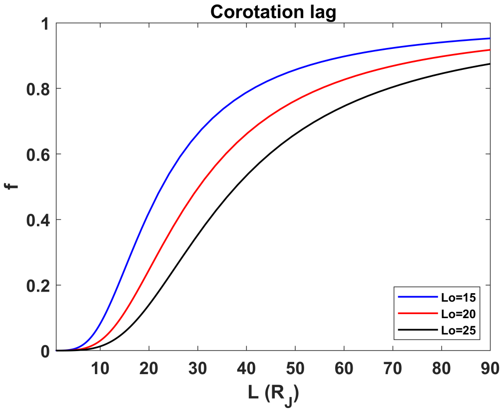

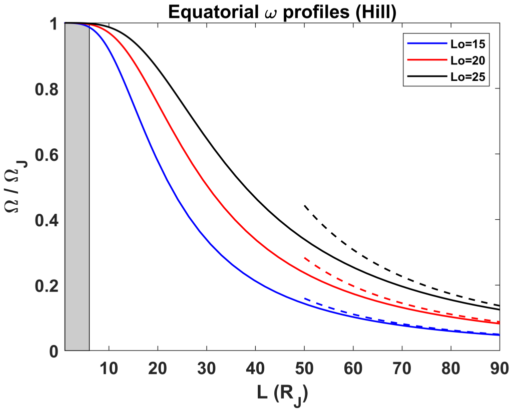

Figure 6: **Top:** Corotation lag ($f = 1 - \omega/\omega_J$) as a function of the equatorial distance for different values of L_o. **Bottom:** Angular velocity in terms of the planetary value, as a function of the equatorial distance for the same values of L_o. The dashed lines show the asymptotic behaviour of Hill's solution obtained using the conservation of angular momentum: ($f \simeq 1 - \pi^{1/2}(L_o/L)^2$). The shaded box represents the corotation region, extending roughly up to the orbit of Io at $6R_J$.

$$\mu_B = \frac{B_r^i(\theta)}{B_{r,dip}^i} \cdot \frac{B_z^{eq}(\rho)}{B_{z,dip}^{eq}} \rho \sin^2\theta \qquad , \tag{25}$$

where the dipolar magnetic field components $B_{r,dip}/, B_{z,dip}$ are also a function of θ and ρ respectively (with a known analytical expression). The first factor $\dfrac{B_r^i(\theta)}{B_{r,dip}^i}$ represents the deviation of the radial magnetic field component from a magnetic dipole. This factor can be approximated with unity, since near the high-latitude ionosphere the magnetic field is predominantly radial and closely follows a dipole profile. In contrast with the radial component, the perpendicular (z) component deviates from the dipole approximation for large equatorial distances, as the magnetodisc profile suggests (see Fig. 2). We can directly calculate this term, using the UCL magnetodisc code.

At this point, it is useful to mention that Hill's equation can be retrieved from Pontius' if we set $\mu_B = 1$ (i.e. no deviation from a magnetic dipole) and use the analytical expression of the mapping function shown above. By extension, for regions near Jupiter, where the magnetic dipole approximation is justified, Hill's prediction for ω is still valid.

Last, we need to connect every point on the magnetodisc (along the equator) with its "magnetic conjugate" at the inner boundary of the solution grid (i.e. the ionosphere) along the same magnetic field line; this is achieved via the "mapping function". Going back to equation 22, we can see that the mapping function has an analytical expression for a simple magnetic dipole: $\cos\theta_i(r) = (1 - 1/L)^{1/2}$. However, due to the expansion of the magnetic potential α, an analytical expression is not always possible. Using the UCL magnetodisc code, we use the magnetic field profile to retrieve numerically the mapping function, following a contour of constant α.

The last assumption we need before applying Pontius' algorithm is to set an upper limit on the corotation distance. Typically, the corotation region is believed to extend up to the orbit of Io ($\sim 6R_J$). In our case, in order to improve the behaviour of the numerical solution and achieve a smoother angular velocity profile, we set as initial condition $f = 0$ at $L = 5.0R_J$.

4.1.1. Update process for ω

Now we can proceed to the update of the angular velocity for a given magnetodisc model. First, we follow Caudal's method (with an initial profile for ω) to obtain a numerical solution for α. Then, we start a second iterative loop where we calculate the Pontius term μ_B and the mapping function. The new profile of ω is then used again to update α. This two-loop process is described by Fig. 7. For simplicity, we will present here results using only the equatorial parameters given by (Caudal, 1986).

An example of an updated angular velocity is shown in Fig. 8 where we plot Hill's and Pontius' solutions for two different cases of hot plasma content. The corotation for both solutions (Hill's or Pontius') is only valid up to $r \lesssim 10R_J$ and then the angular velocity decreases; the difference is evident after $40R_J$. Applying Ferraro's law, we can also create a 2-dimensional map of the angular velocity, shown in Fig. 9.

Although the addition of μ_B captures the deviation of the computed magnetic field from the dipole case, it does not strictly originate from first principles; it is an empirical method to incorporate the magnetodisc in the analysis. As a consequence, Pontius' equation does not - in general - lead to a conservation law for the angular momentum for the length scales we examine here (Fig. 10). The exact behaviour of the angular momentum profile changes significantly with K_h, but it can be seen on every comparison between models with different R_{mp} , K_h using the two angular velocity methods (Hill's and Pontius').

The numerical process for the calculation of ω follows exactly the same pattern as the one used in the original Caudal's method for α:

$$\omega = \lambda_{i-1}\omega_{i-1} + \lambda_i\omega_i \quad , \tag{26}$$

where ω is the initial condition used in the next iteration $(i+1)$ and λ_{i-1},λ_i are the fractions of the "old" (ω_{i-1}) and "new" (ω_i) solution respectively. Similar to the previous case (calculation of α), the coefficients $\lambda_{i,i-1}$ can be in principle any number in $[0,1]$, subject only to the restriction $\lambda_{i-1} + \lambda_i = 1$.

Each relaxation process stops when the relative difference between $(\omega_i -$

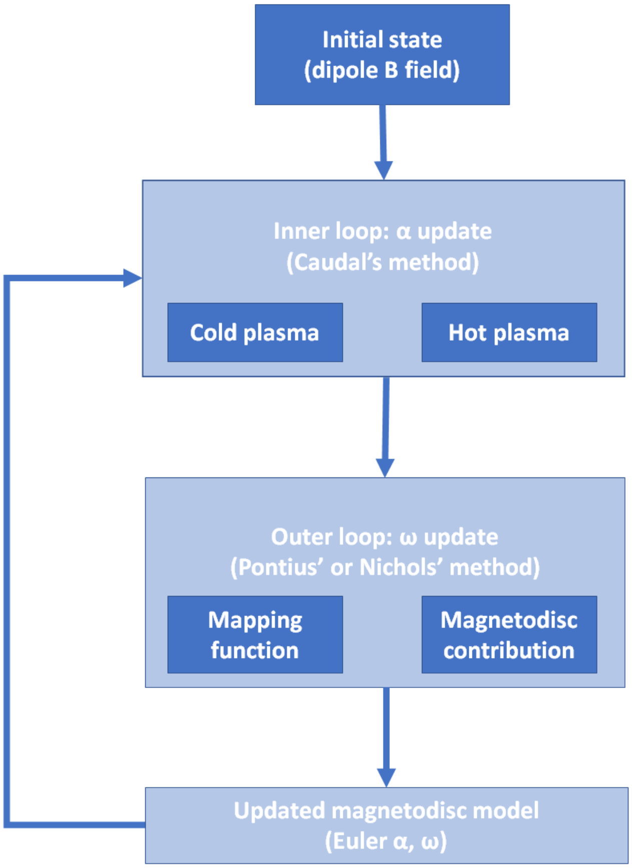

Figure 7: A simple flowchart of the two iterative procedures in an "inner-outer" loop scheme. First, we set up the initial conditions; then Caudal's scheme (treating separately the cold and hot plasma) is used to calculate a new profile for α (inner loop), which is halted when an effective tolerance of 10^{-2} between iterations is achieved. The final state of the inner loop serves as an initial condition for the update of the angular velocity (outer loop). The outer loop uses Pontius' method to produce a relaxed profile of ω. The outer loop ends when a certain accuracy is achieved. For completeness, see also Figure 4 from Caudal (1986), which describes the inner loop of the flowchart.

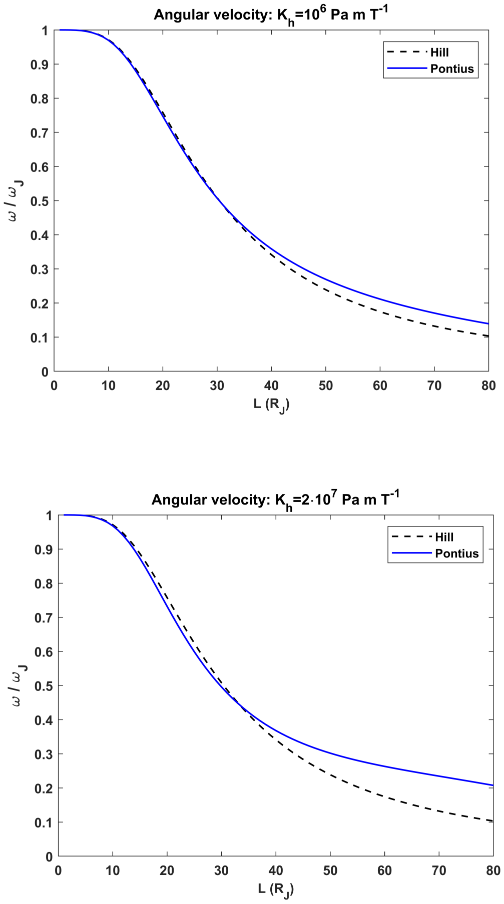

Figure 8: Comparison between Hill's and Pontius' solutions for the angular velocity ω (dashed and solid lines respectively), for models with $K_h = 10^6$ Pa m T^{-1} (*top*) and $K_h = 2 \cdot 10^7$ Pa m T^{-1} (*bottom*), using Voyager-like conditions. The updated solution (Pontius') deviates from Hill's prediction for distances roughly larger than $40R_J$, whereas for smaller distances the difference $|\delta\omega| \lesssim 4 \cdot 10^{-2}$. For distances smaller than $40R_J$, the magnetodisc field is weaker, which leads to smaller values of ω compared to Hill's prediction.

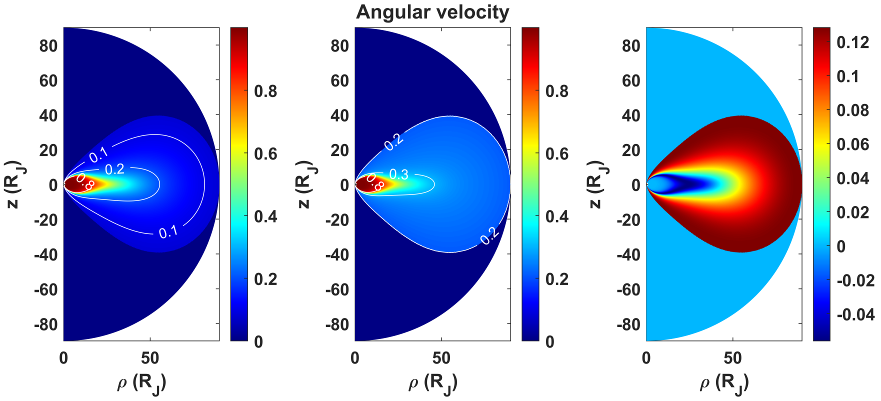

Figure 9: Angular velocity map according to Hill's solution (left) and Pontius' method (middle), using Ferraro's isorotation law. The difference between the two profiles is shown on the right panel.

$\omega_{i-1})/\omega_i$ (same for α) becomes smaller than a user-defined threshold. We remind that this threshold depends on (or better, is not independent of) the mixing factor λ_i; similarly to the calculation of α, we set the effective tolerance to 10^{-2}.

Choosing a higher fraction of the new solution (λ_i, ν_i) leads to a faster relaxation (fewer repetitions of the "inner" and/or the "outer" loop), although again in some cases it is advisable to start with a smaller λ_i, ν_i value (at the expense of more iterations).

An additional constraint here is that the mixing factors for the Euler potential α (ν_i) and the angular velocity ω (λ_i) must not be significantly different, especially in models with large hot plasma content. In other words, it is necessary to use a similar number of iterations for α and ω to ensure numerical stability.

4.2. Effects on the force balance

As mentioned earlier, one of the key assumptions of Caudal's scheme is the total force equilibrium between the magnetic force, the (total) thermal pressure gradient and the centrifugal force. The choice of a specific profile for the angular velocity (e.g. Hill's) as an initial condition also determines the centrifugal

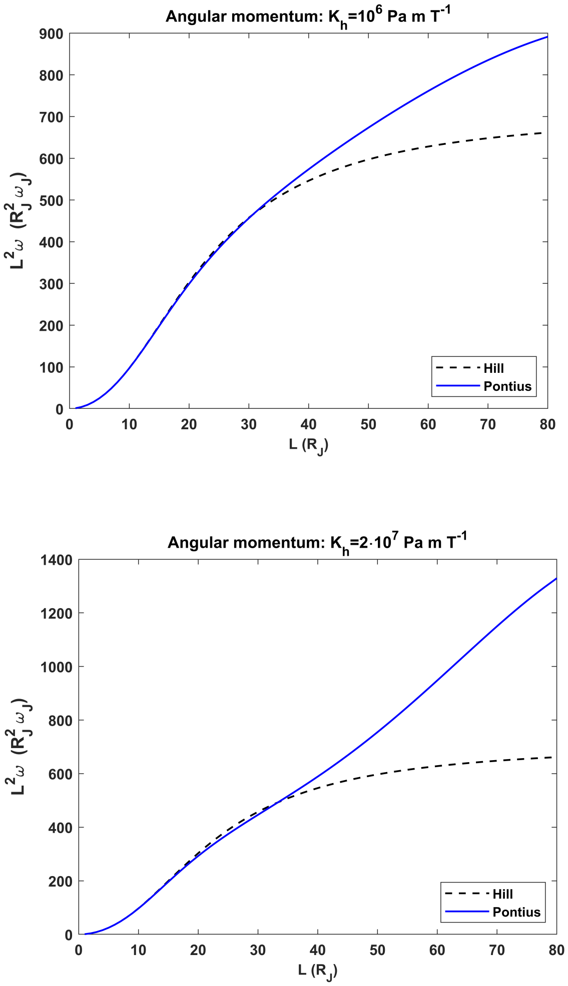

Figure 10: Dimensionless angular momentum for the models of Fig. 8. Hill's angular velocity profile (black, dashed) assumes a constant angular momentum at distances far from the planet; this is confirmed as the solution gradually reaches a plateau after $L \sim 60R_J$. This is not the case, however, for Pontius' solution (blue, solid).

force and consequently the total force equilibrium. If the angular velocity does not follow Hill's profile, then the ratio between these three forces is modified during the iterative process to ensure equilibrium. Nichols (2011) discussed the implications of the presence of the magnetodisc on the angular velocity and thus the centrifugal force. For a description of Nichols' angular velocity update, see Appendix A.

We present in Fig. 11 the centrifugal force after the angular velocity is updated using $K_h = 10^6$ Pa m T^{-1} and $K_h = 2 \cdot 10^7$ Pa m T^{-1}. Using the numerical solutions obtained from Pontius' differential equations, the centrifugal force increases by at least a factor of two in the middle and outer magnetosphere compared to the profile corresponding to Hill's dipole solution. Thus, the magnetic force and the thermal pressure are modified accordingly.

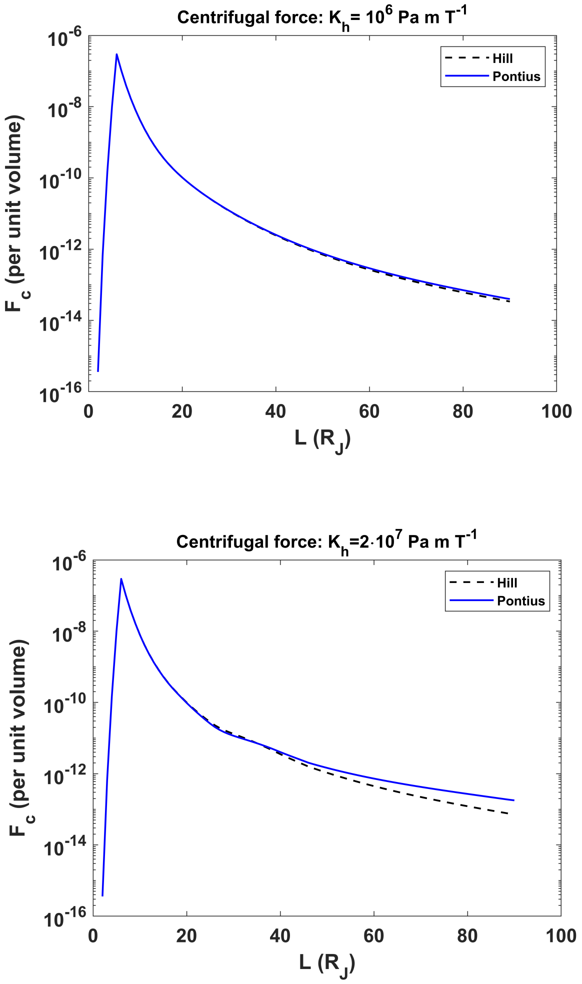

Figure 11: Centrifugal force per unit volume, for Hill and Pontius solutions for ω. Showing cases with $K_h = 10^6$ (*top*) and $2 \cdot 10^7$Pa m T^{-1} (*bottom*). The updated angular velocity profile leads to a larger centrifugal force compared to the dipole prediction.

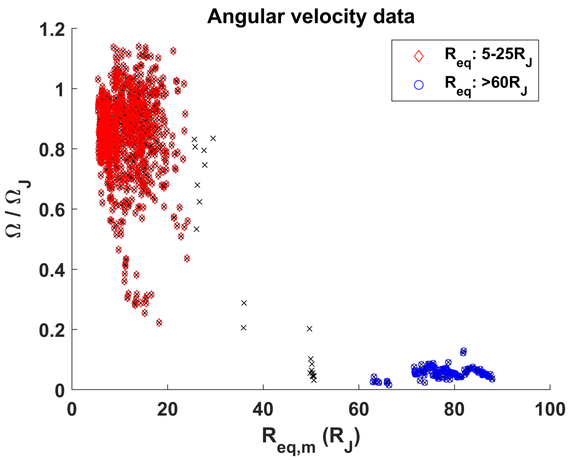

Figure 12: **Galileo**PLS data divided in two regions. The black marks represent the complete data set, the red and blue marks the data points at a distance $5 - 20R_J$ and $> 60R_J$ respectively. The data points in the middle magnetosphere are ignored, since there are very few to obtain an accurate fit.

5. Comparison with selected spacecraft observations

5.1. Angular velocity profile

In order to determine the validity of the updated angular velocity profile, we compare the numerical solution with plasma moments obtained from the Galileo Plasma Science Experiment (PLS) data. In particular, we focus on the data used in (Bagenal et al., 2016).

The original data set was given in "jovigraphic" spherical coordinates, so initially we performed a transformation to magnetic coordinates. We also filter out any data obtained at distances $z > 5R_J$ from the magnetic equator and use only data from the dayside (facing the Sun). This results in a data set with roughly 1600 points. Since there are very few data points in the middle magnetosphere, we focus only on two regions where the measurements are clustered: between 5-25R_J and $60 - 90R_J$. The distribution of the data points along the magnetic equator is shown in Fig. 12.

These regions are divided in uniform bins of the same size (for each region). We then compare the numerical solution with the median of each bin, taking into account that there is no realistic comparison in the middle magnetosphere. This choice results in an uneven number of points in each bin; however, the general behaviour of the median does not change much for the inner magnetosphere (except close to $25R_J$). The data points for the outer magnetosphere are relatively few and in order to keep the same number of points per bin, they would have to be treated as one bin.

In Fig. 13 we present the data points and the comparison with the numerical solutions. At first, we notice that both Hill's and Pontius' solutions do not agree well with the observed values of the angular velocity. However, the trend of the measured values does not agree with the corotation assumption near the orbit of Io, leading to a systematic error. One possible solution would be to rerun the magnetodisc code, using as an initial condition $\omega_o = 0.9$ at the orbit of Io, the value obtained via interpolation from the data. However, the numerical solution is driven by the corotation assumption, which will finally result in the same disagreement; experiments with $\omega_o < 1$ showed that the angular velocity quickly returns to 1 near Io. Unless a very small value of ω_o is used as an initial condition (which is not a physical assumption), the radial currents will tend to accelerate the plasma in this region towards corotation.

Another source of uncertainty, especially for large distances is the true value of L_o. In Caudal's theory and our numerical implementation it is treated as a constant (L_o=20) but, as shown in the discussion of Hill's theory, there is a significant effect on the final angular velocity profile (Fig. 6). Different values of L_o could potentially lead to better agreement. The limitations in energy resolution of Galileo also introduce an error since different ion species are not always effectively separated (Bagenal et al., 2016).

Note that the work of Bagenal et al. (2016) only provides plots and fits for plasma parameters from Galileo PLS data out to $30R_J$. However, the Galileo PLS database referenced in our paper and plotted in Figure 13 both extend to $\sim 90R_J$. These plasma parameters are derived assuming an average mass-to-charge ratio of heavy ions, based on physical chemistry modeling of the Io plasma torus. While this assumption is probably valid in the plasma sheet out

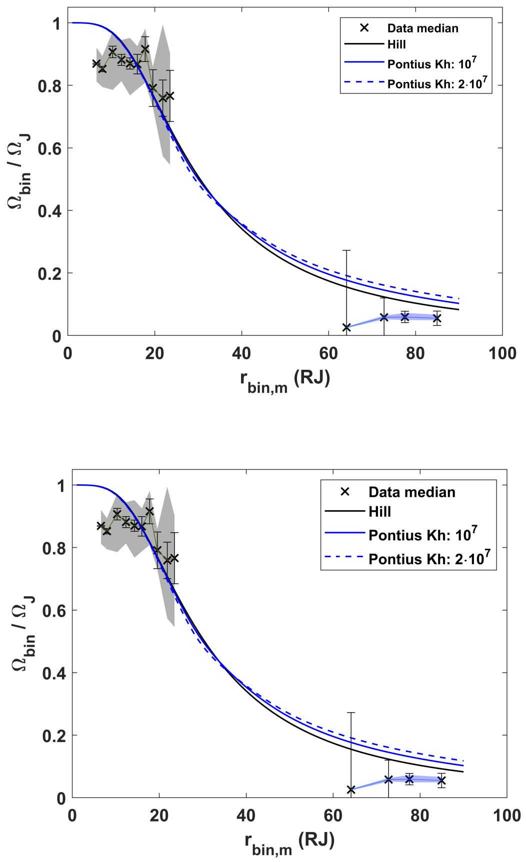

Figure 13: Comparison between Hill (red) and Pontius' (blue) solutions (for different K_h values) and Galileo PLS data. The median of each bin is given with a black cross, using N_1, N_2=(10,4]) bins (top) and N_1, N_2=(15,6) bins (bottom) for the first and second data group respectively. The shaded region represents the 1st and 3rd quantile.

to $\sim 40 R_J$, the ions between $60 - 90 R_J$ likely have a significant contribution of protons and the heavy ions may be above the energy range of the instrument. The azimuthal flow speeds in this region are likely underestimated, therefore, by a factor of a few (personal communication Fran Bagenal and Rob Wilson).

A re-analysis of the Voyager 1 and 2 data by Bagenal et al. (2017), using a mean mass-per-charge based on chemistry models, provided more accurate information on the ion composition. The results where then used by Dougherty et al. (2017) to derive the plasma properties. Of particular interest for our study are the profiles of the azimuthal velocity, given in Figure 3 (Dougherty et al., 2017). The authors compare the Voyager data with a existing theoretical predictions for the angular velocity, up to 40 R_J. For the same range, the profiles of ω obtained from our models are in good agreement with the predictions of Hill (1980); Nichols and Cowley (2004) show over the Voyager data. We emphasise that due to the dependence of the solution for ω on L_o, small differences are expected.

Last, we compare the azimuthal velocity, shown in Fig. 14, with the profiles provided by the numerical simulations of (Chané et al., 2013). These simulations used different parameters (e.g. Io torus mass loading rate, Pedersen conductivity) to create models of the Jovian magnetosphere. Although a direct comparison is not possible, as in our case the mass loading rate and the conductivity are expressed via the L_o parameter, the order of magnitude and the trend is in good agreement with models A and B shown in Fig. 7 of (Chané et al., 2013).

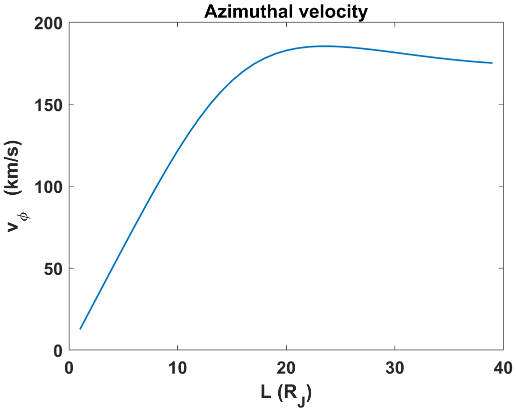

Figure 14: Azimuthal velocity up to an equatorial crossing distance of $40R_J$. The profile and the order of magnitude are close to the solutions obtained by the simulations of (Chané et al., 2013)

.

5.2. *Equatorial current density*

We now compare the equatorial, azimuthal current density obtained from the magnetodisc code, using both Caudal-like (or Voyager-like) and Galileo-like initial conditions, with profiles obtained from various missions. We will focus on models with Hill's profile for the angular velocity, as the update does not significantly modify the equatorial current.

We remind that (Connerney et al., 1981a) proposed that $J_\phi \sim \rho^{-1}$ (using Voyager data) and Caudal's model predicts $J_\phi \sim \rho^{-1.2}$. Furthermore, (Alexeev and Belenkaya, 2005) used a faster decreasing function, $J_\phi \simeq \rho^{-2}$. One of the most recent profiles for J_ϕ was provided by (Connerney et al., 2020), using parameters obtained from Juno data. We compare the output from the numerical model with these profiles in Fig. 15.

Some differences do exist between these profiles, while the order of magnitude is captured sufficiently. Both the Voyager and Galileo models show a fast decrease in the azimuthal current, more consistent with (Alexeev and Belenkaya, 2005). In Figure 8g from Nichols et al. (2015), we can see a qualitative agreement with our Galileo runs, in terms of the maximum current density value

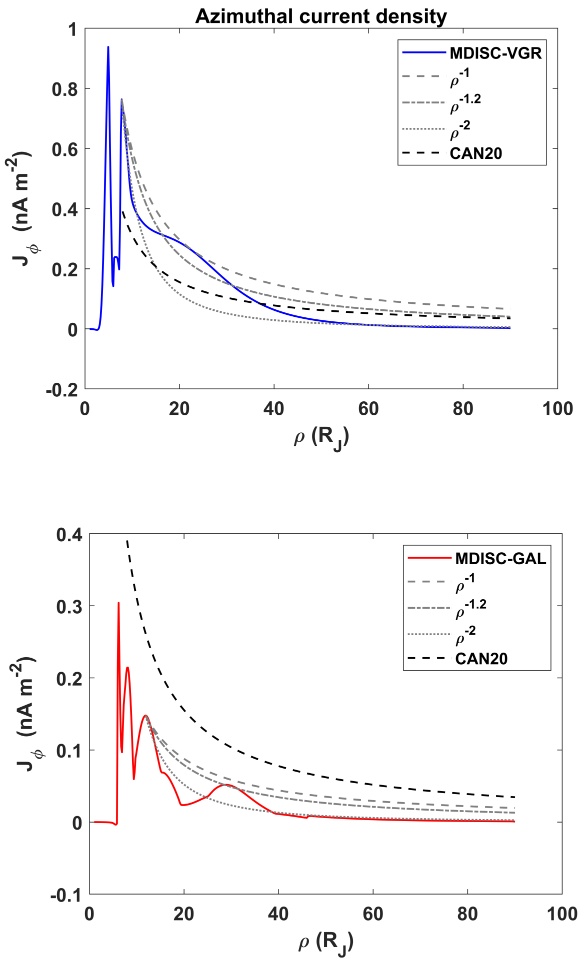

Figure 15: Comparison between the azimuthal current density profile along the equator from the magnetodisc models (solid lines) - using Voyager (**top**) or Galileo (**bottom**) initial conditions, with various scaling profiles from (Connerney et al., 1981a) ($J_\phi \simeq \rho^{-1}$), (Caudal, 1986) ($J_\phi \simeq \rho^{-1.2}$) and (Alexeev and Belenkaya, 2005) ($J_\phi \simeq \rho^{-2}$). These are scaled to the value of J_ϕ at a distance where the profile begins to be smooth ($\sim 7.5 R_J$ and $\sim 11 R_J$for Voyager or Galileo models respectively. Last, we show the profile of (Connerney et al., 2020) based on Juno data. The values from the Galileo model are in qualitative agreement with Figure 8g from Nichols et al. (2015)

.

($\sim 0.1\ nA\ m^{-2}$); in the same figure, the authors provide a the relative contribution from each component. A direct, quantitative comparison is not possible since our model does not include pressure anisotropy.

(Khurana, 2001) and (Lorch et al., 2020) calculated the height integrated azimuthal current using the formula:

$$J'_\phi = \frac{1}{\mu_o}\left(2\frac{\partial B_\rho}{\partial z} - 2w\frac{\partial B_z}{\partial \rho}\right) \tag{27}$$

where w is the half-thickness of the current disk. The first term was estimated from B_{rho} components in the lobes adjacent to a current sheet crossing while the second term was estimated by fitting the following function to measurements of B_z at the centre of the current sheet and differentiating.

$$B_z = \frac{a}{\rho} + \frac{b}{\rho^2} + \frac{c}{\rho^3} \tag{28}$$

where a,b,c are constants obtained from fitting the magnetic field data; in particular, (Khurana, 2001) used data from Galileo while (Lorch et al., 2020) used data from all available missions up to July 2018.

In Fig. 16 we compare the fits for the differenced B_z (obtained by subtracting the internal potential field) with the output from the magnetodisc code (plot on top) and the azimuthal current density as predicted from the code and the fits (plot in bottom). We notice that there is a difference between the fitted B_z function and the profile from magnetodisc code which, in turn, appears also in the azimuthal current density profiles. Instead of the height integrated current density, we calculate numerically the quantity $J_\phi = \frac{1}{\mu_o}\left(\frac{\partial B_\rho}{\partial z} - \frac{\partial B_z}{\partial \rho}\right)$, using Voyager or Galileo based models. Since the functions provided by Khurana (2001); Lorch et al. (2020) take into account measurements from different local time sectors, we also compare these fits with a magnetodisc model using a magnetopause distance of $R_{mp} = 150R_J$ (appropriate for the dusk side). This provides a better agreement with the fitted functions.

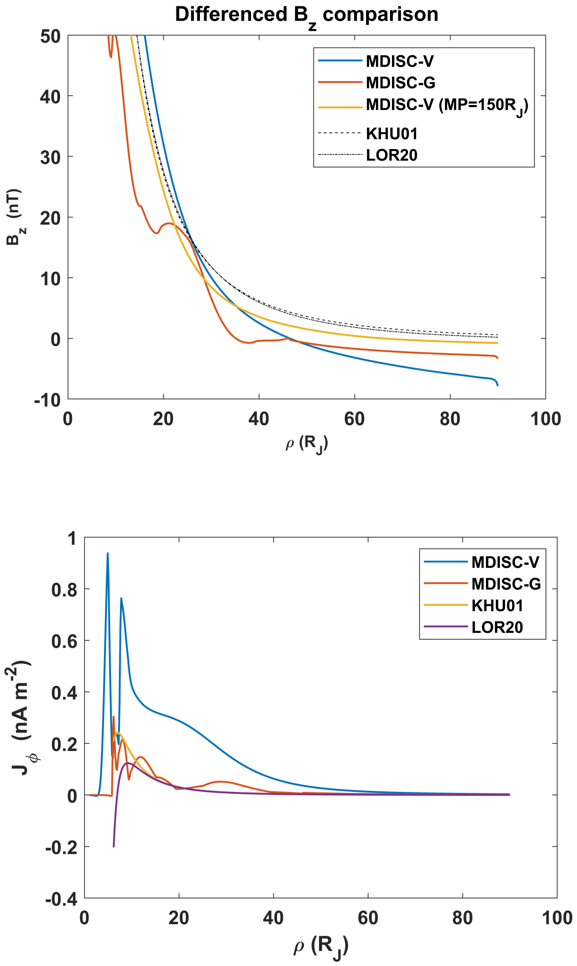

Figure 16: **Top:** Comparison of the differenced B_z, using magnetodisc models with Voyager (blue) or Galileo (red) conditions. The fits of (Khurana, 2001), (Lorch et al., 2020) are shown with dashed and dot-dashed lines. The yellow line represents the differenced B_z from a model using Voyager conditions but setting the magnetopause distance at 150 R_J. **Bottom:** Similar to Fig. 15, comparing now the magnetodisc output with (Khurana, 2001; Lorch et al., 2020).

6. Conclusions

We report on an updated version of the UCL/AGA code, a numerical implementation of Caudal's theory (Caudal, 1986) for the construction of models of the Jovian magnetosphere. The assumptions of the Caudalian scheme include axisymmetry, isotropic plasma and force balance between the magnetic force, the pressure gradient (including contribution from hot plasma) and the centrifugal force. All physical quantities are derived from the calculation of the Euler potential α. In Caudal's original work, the equatorial initial conditions necessary for the numerical iterations are obtained from Voyager data.

In this work, we investigated the following topics:

- Implement newer Galileo profiles (Bagenal and Delamere, 2011; Bagenal et al., 2016) for the equatorial plasma conditions: density, temperature and flux tube content. Include new profiles for the energetic particle pressure (Mauk et al., 2004).
- Include an angular velocity correction algorithm based on Pontius' method Pontius (1997), which accounts for the presence of the magnetodisc.
- Compare the corrected angular velocity with Galileo data.
- Compare the output from Voyager or Galileo based models with different current profiles.
- Numerical tests in terms of grid and step size.

A summary of each topic is given in the following paragraphs.

The equatorial number density distribution and the temperature are obtained from empirical fits and are now smooth functions, in contrast with the step functions originally used by Caudal from Voyager data. The number density behaviour is quite similar in both Voyager and Galileo data, but with a difference of approximately one order of magnitude for large equatorial radii. The equatorial temperature (or equivalently, the scale height) is systematically larger in the Galileo data (due to the ability to detect higher energies), reaching an asymptotic value of $\sim 10^3$ eV around $20R_J$; the profile used by Caudal shows a continuous increase in temperature. Regarding the hot plasma pressure, the Galileo data indicate a smaller hot plasma content compared to the Voyager profiles.

The second addition is a numerical implementation of Pontius' method to our existing numerical scheme to calculate the angular velocity profile in a consistent way i.e. taking into account the magnetodisc. First, we construct the dayside magnetosphere, including the magnetodisc based on Caudal's theory. Up to this point the angular velocity is described by Hill's solution, consistent with a dipole. Using the resulting relaxed state, we then update the equatorial angular velocity, solving numerically Pontius' differential equation for the corotation lag.

Our results show that initially Hill's and Pontius' solutions coincide; this is consistent with the magnetic field profile, which is approximately a dipole for small distances. The rigid corotation breaks down roughly at $10R_J$ for both solutions, with small differences between them visible up to $40R_J$. A significant increase in the "updated" angular velocity compared to Hill's dipole solution is evident after $40R_J$. We tested the angular velocity profiles for both methods against plasma moments from Galileo and found that in the inner magnetosphere, both methods produce sufficiently accurate results. The results are less clear, however, in the outer magnetosphere due to a combination of lack of data and uncertainties in the physical properties of the plasma itself (e.g. the L_o parameter, which acts as a proxy for certain physical parameters).

The angular velocity profile obtained from Pontius' equation leads to an increase in the centrifugal force experienced by the plasma on the equator, which may have implications for the total behaviour of the system and the compressibility of the Jovian magnetosphere. This particluar application will be examined in future work.

Comparing the azimuthal current density along the equator, we found that both choices of initial conditions lead to a fast decrease with equatorial distance, close to ρ^{-2}, similar to the case of (Alexeev and Belenkaya, 2005). The azimuthal current density profiles calculated by Khurana (2001); Lorch et al.

(2020) seem to be a better match for our Galileo models. This can also be seen in the profiles of the differenced B_z, as the order of magnitude predicted by our models (again, especially when using Galileo conditions) is in good agreement with the third order fits shown in Khurana (2001); Lorch et al. (2020).

We also tested the code for grids of different resolution and for different number of iterations in the calculation of α and ω. We found that for a typical magnetopause radius of $R_{mp} \simeq 80R_J$, even small grids (e.g. with $(\rho, \cos\theta)$ grid size of (200x201) points, or a resolution of 0.4 Jovian radii) can provide a satisfactory model if Hill's solution is used. Models with significant hot plasma population and/or an update in angular velocity may require a finer grid. The numerical tests can be found in the appendix.

We aim to further update the code, implementing newer profiles from Juno data. This will enable us to produce realistic models of the Jovian magnetosphere for different eras and examine different characteristics, such as its compressibility and the motion of charged particles in the modified magnetic field. The algorithm used to update the angular velocity may also be adapted for the magnetosphere of Saturn.

Data availability

The authors are willing to share the models of the Jovian magnetosphere if a reasonable request is made. Specific models will be uploaded in a repository over the next months.

Acknowledgements

Funding: This work was supported by UK STFC (Science and Technology Facilities Council) Consolidated Grant ST/S000240/1 (UCL-MSSL, University College London-Mullard Space Science Laboratory, Solar System). C.S. Arridge was supported by a Royal Society Research Fellowship under grant number UF160697.

We thank R.J. Wilson for his help regarding the Galileo plasma moments. Information on the Galileo PLS data can be found at: https://doi.org/10.17189/1521148 and was used in Bagenal et al. (2016).

([dataset] Wilson, R. J, "Galileo Orbiter Plasma Science Experiment Jupiter Fitted Parameters Bundle", https://pds-ppi.igpp.ucla.edu/search/view/?id=pds://PPI/go-pls-jup-fitted-parameters).

We would also like to thank Fran Bagenal and Jonathan Nichols for the useful discussions and their suggestions.

Appendix A. Nichols' method for angular velocity update

An alternative (and similar) method to update the angular velocity was provided by (Nichols and Cowley, 2004; Nichols et al., 2015). The equation that now determines the angular velocity profile is:

$$\frac{d\omega}{dL} = \frac{2}{L}\Big(\frac{4\pi\Sigma_P^* B_o^2 R_J^2 F_e B_{ze}(1-\omega)}{\dot{M}} \; - \; \omega\Big) \tag{A.1}$$

where again $\dot{M}$ is the mass outflow rate, Σ_P^* is the effective Pedersen conductance and F_e, B_{ze} are the equatorial magnetic flux and equatorial magnetic field respectively.

There are some subtle differences between the equations 22,24 and A.1 that we should highlight in advance: the polar magnetic field strength is assumed to be equal to $2B_J$ in Nichols and Cowley (2003, 2004). Fiducial profiles for the equatorial magnetic field and the flux function are given in Nichols and Cowley (2004):

$$B_{ze} = -\Bigg\{B_o\Bigg(\frac{R_J}{\rho})^3 exp\Bigg[-\frac{\rho}{\rho_o}^{5/2}\Bigg] + A\Bigg(\frac{R_J}{\rho}\Bigg)^m\Bigg\} \tag{A.2}$$

$$F_e = F_\infty + \frac{B_J R_J^3}{2.5\rho}\Gamma\Bigg[-2/5, \Bigg(\frac{\rho}{\rho_o}\Bigg)^{5/2}\Bigg] + \frac{A}{m-2}\Bigg(\frac{R_J}{\rho}\Bigg)^{m-2} \tag{A.3}$$

where $B_o = 3.335 \cdot 10^5$nT, $\rho_o = 14.501 R_J$,$A = 5.4 \cdot 10^4$nT,$m = 2.71$,F_e is the flux function, F_∞ is the value of the flux function at infinity, $\Gamma(x, y)$

is the incomplete Gamma function and $m = 2.71$ (obtained from the equatorial magnetic field profile). This profile reproduces the CAN model values for the equatorial magnetic field and the flux function at a cylindrical equatorial distance $\rho = 5R_J$.

The flux function can then be found via the formula:

$$\sin\theta_i = \sqrt{\frac{F_e}{B_J R_J^2}} \tag{A.4}$$

In addition, the effective Pedersen conductance, defined as $\Sigma_P^* = (1-k)\Sigma$, corrects the true value (Σ) due to the slippage from the (neutral) atmosphere from rigid corotation using the parameter k. For simplicity, we can choose, following (Nichols and Cowley, 2003, 2004) $k = 0.5$, meaning that the true value is halved. This is not the case for Pontius' method, where the Pedersen conductance is included in the calculation of L_o and is thus obtained from the magnetodisc model output.

A comparison between the equatorial magnetic field and the mapping functions for Hill's, Pontius' and Nichols' fiducial profiles (equations A.2,A.3, as in Nichols and Cowley (2004)) is shown in Fig. A.17.

In the following analysis, we used for simplicity the initial conditions given in (Caudal, 1986) (Voyager conditions). For completeness, compare with Figure 2 from (Nichols and Cowley, 2004), showing details on the CAN model.

Overall, there are some (usually minor) differences to be expected for the angular velocity profile obtained with Pontius' and Nichols' algorithms, depending (as we will show) on the value of K_h. We present the solutions for various models (shown in Table B.1) in Fig. A.18.

Notice that in Figure 6a of Nichols et al. (2020), the equatorial magnetic field from the output of a magnetodisc model is shown, which is very similar to the profiles from the cases we discuss here. See also Figure 7 of Nichols et al. (2020) where models of the magnetosphere with and without enhancement of hot plasma pressure are discussed; the updated angular velocity profiles are very similar to the ones obtained from our models. Figure 11 from Nichols et al. (2015) is showing similar behaviour for ω as well.

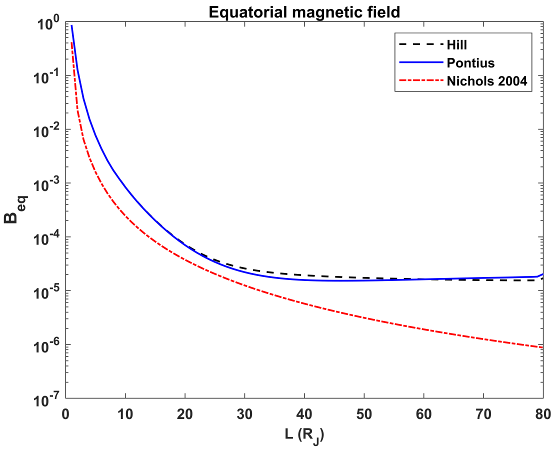

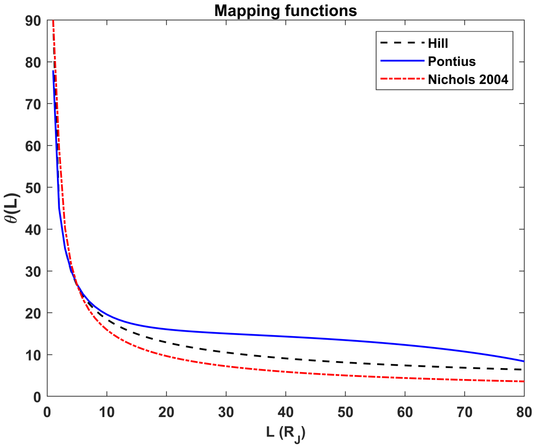

Figure A.17: **Top:** Equatorial magnetic field in log scale, normalized to the planetary value in models using Hill's, Pontius' and Nichols' methods respectively, for the update of angular velocity. **Bottom:** Comparison between the mapping function for the same models. The Nichols' cases refer to the fiducial models from Nichols and Cowley (2004).

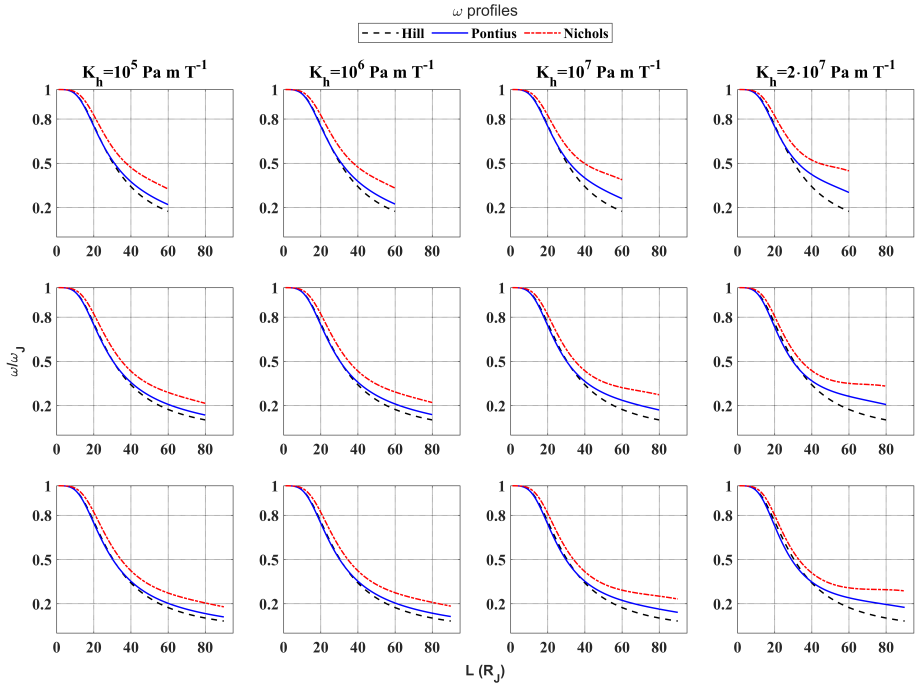

Figure A.18: Angular velocity profiles for every model in Table B.1. **Left to right:** Models with larger K_h values. **Top to bottom:** Models with larger magnetopause radius R_{mp}

We opted to use Pontius' algorithm in our code since it provides a convenient method to calculate the difference between the dipole and magnetodisc fields. Although it is beyond the scope of this work, we note that Nichols' algorithm has been successfully used in models with plasma pressure anisotropy Nichols et al. (2015).

Appendix B. Numerical tests

In this section, we present some basic numerical tests we performed to determine the robustness of the updated code and the angular velocity update algorithm in particular. These tests focus on the grid resolution and provide more details about the "mixing" procedure used in the update routine.

A description of the models used in the following analysis are shown in B.1. Each model is characterized by the magnetopause distance R_{mp}, the hot plasma content index K_h and the solver used for the angular velocity update. We provide also the necessary number of iterations that were performed in order to obtain a solution with a desired accuracy, which is linked to the factor ν_i used for the "intermediate" solution.

Appendix B.1. Grid size

First we will examine the behaviour of the algorithms for different choices of grid size. In order to avoid extremely large hot plasma populations and represent an average state of the Jovian magnetosphere, we select model H8 from Table B.1, thus $K_h = 2 \cdot 10^7$Pa m T^{-1} and $R_{mp} = 80R_J$.

We create different versions of the model, using a Cartesian box with dimensions $(r, \cos\theta)$ from 200x201 to 600x601. These choices provide a sufficient level of detail for the general characteristics of the magnetosphere. The relative error in the equatorial α for each grid size (with respect to the finest grid) is always smaller than 10^{-2}, as shown in Fig. B.19.

Table B.1: Key parameters for every model used to test the angular velocity update algorithms. For the “Hill” models, there is no actual solver involved for the angular velocity, as it corresponds to the value obtained for a dipole. For models using the Pontius’ method, more steps are required as we examine systems with larger K_h. All cases use the Voyager profiles for the equatorial initial conditions.

Name	Solver type	R_{mp} (R_J)	K_hPa m T^{-1}	Grid size	ν_i	λ_i	# iterations (ω)
H1	Hill	60	10^5	500X501	0.25	0.25	-
H2	Hill	60	10^5	500X501	0.25	0.25	-
H3	Hill	60	10^5	500X501	0.25	0.25	-
H4	Hill	60	10^5	500X501	0.25	0.25	-
H5	Hill	80	10^5	500X501	0.25	0.25	-
H6	Hill	80	10^6	500X501	0.25	0.25	-
H7	Hill	80	10^7	500X501	0.25	0.25	-
H8	Hill	80	$2 \cdot 10^7$	500X501	0.25	0.25	-
H9	Hill	90	10^5	500X501	0.25	0.25	-
H10	Hill	90	10^6	500X501	0.25	0.25	-
H11	Hill	90	10^7	500X501	0.25	0.25	-
H12	Hill	90	$2 \cdot 10^7$	500X501	0.25	0.25	-
P1	Pontius	60	10^5	500X501	0.25	0.25	13
P2	Pontius	60	10^5	500X501	0.25	0.25	13
P3	Pontius	60	10^5	500X501	0.25	0.25	14
P4	Pontius	60	10^5	500X501	0.25	0.25	15
P5	Pontius	80	10^5	500X501	0.25	0.25	13
P6	Pontius	80	10^6	500X501	0.25	0.25	13
P7	Pontius	80	10^7	500X501	0.25	0.25	15
P8	Pontius	80	$2 \cdot 10^7$	500X501	0.25	0.25	15
P9	Pontius	90	10^5	500X501	0.25	0.25	13
P10	Pontius	90	10^6	500X501	0.25	0.25	13
P11	Pontius	90	10^7	500X501	0.25	0.25	15
P12	Pontius	90	$2 \cdot 10^7$	500X501	0.25	0.25	15
N1	Nichols	60	10^5	500X501	0.25	0.25	17
N2	Nichols	60	10^5	500X501	0.25	0.25	17
N3	Nichols	60	10^5	500X501	0.25	0.25	17
N4	Nichols	60	10^5	500X501	0.25	0.25	17
N5	Nichols	80	10^5	500X501	0.25	0.25	17
N6	Nichols	80	10^6	500X501	0.25	0.25	17
N7	Nichols	80	$1 \cdot 10^7$	500X501	0.25	0.25	17
N8	Nichols	80	$2 \cdot 10^7$	500X501	0.25	0.25	17
N9	Nichols	90	10^5	500X501	0.25	0.25	17
N10	Nichols	90	10^6	500X501	0.25	0.25	17
N11	Nichols	90	$1 \cdot 10^7$	500X501	0.25	0.25	17
N12	Nichols	90	$2 \cdot 10^7$	500X501	0.25	0.25	17

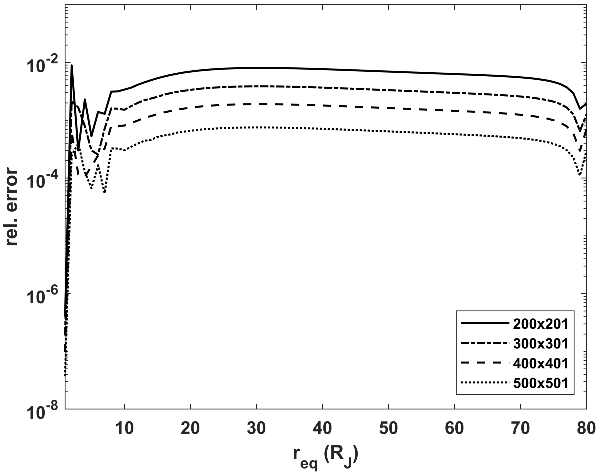

Figure B.19: Relative error in the equatorial potential α, calculated with respect to a grid with size 600 × 601.

Appendix B.2. Effects of "mixing" coefficients (number of iterations)

We will now investigate the differences in the updated solution of ω using a different number of iterations (i.e. λ_i). We select model P8 ($K_h = 2 \cdot 10^7$Pa m T^{-1} and $R_{mp} = 80R_J$), exploring three choices of the mixing coefficient: $\lambda_i = 0.25$, $\lambda = 0.3$ and $\lambda_i = 0.5$. A visualization of the relaxation process is shown in Fig. B.20. The final ω profile is approximately the same, with an absolute relative error between the choices between $\lambda_i = 0.5$ and $\lambda_i = 0.25$ being smaller than $6 \cdot 10^{-4}$.

The difference between the two choices is quite small and thus justifies the use of a "large" fraction (e.g. $\lambda_i = 0.5$) of the new solution when updating the angular velocity. However, special attention is required when the grid resolution is small (e.g. 200x201) and/or the fractions λ_i and λ_{i-1} are considerably different with the corresponding fractions ($\nu_{i,i-1}$) for the update of α. Since ω and α are not updated simultaneously, different choices of λ may result in steep gradients, which make the numerical schemes unstable.

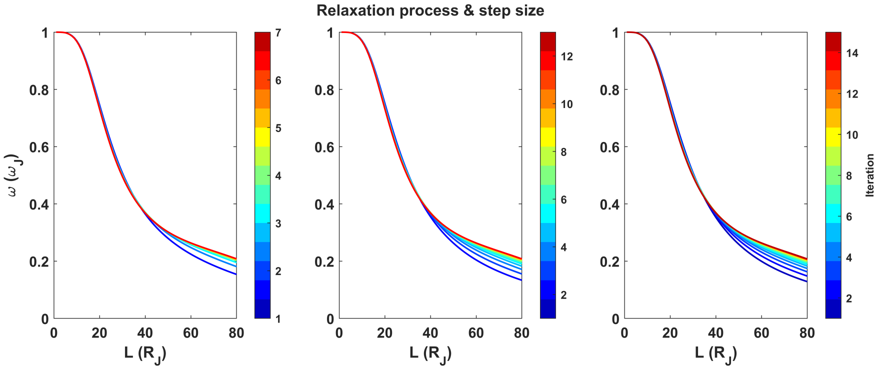

Figure B.20: Updating the angular velocity using Pontius' method with different step sizes, for a model with $R_{mp} = 80R_J$, $K_h = 2 \cdot 10^7$ Pa m $\mathrm{T}^{-}1$. Showing here values of λ_i =0.5,0.3 and 0.25 seen from left to right. The choice of the mixing coefficient λ_i determines the number of iterations, which are 7,13 and 15 respectively. In all cases, the iteration stops when the desired threshold is achieved. The difference in the final solution between the smaller and the larger step size cases is $\delta\omega < 6 \cdot 10^{-4}$.

References

Achilleos, N., Guio, P., Arridge, C.S., 2010. A model of force balance in Saturn's magnetodisc. MNRAS 401, 2349–2371. doi:`10.1111/j.1365-2966.2009.15865.x`, `arXiv:0909.1514`.

Alexeev, I.I., Belenkaya, E.S., 2005. Modeling of the jovian magnetosphere. Annales Geophysicae 23, 809–826. URL: `https://angeo.copernicus.org/articles/23/809/2005/`, doi:`10.5194/angeo-23-809-2005`.

Bagenal, F., Delamere, P.A., 2011. Flow of mass and energy in the magnetospheres of Jupiter and Saturn. Journal of Geophysical Research (Space Physics) 116, A05209. doi:`10.1029/2010JA016294`.

Bagenal, F., Dougherty, L.P., Bodisch, K.M., Richardson, J.D., Belcher, J.M., 2017. Survey of Voyager plasma science ions at Jupiter: 1. Analysis method. Journal of Geophysical Research (Space Physics) 122, 8241–8256. doi:`10.1002/2016JA023797`.

Bagenal, F., McNutt, R.L., Belcher, J.W., Bridge, H.S., Sullivan, J.D., 1985. Revised ion temperatures for Voyager plasma measurements in the Io plasma torus. J. Geophys. Res. 90, 1755–1758. doi:`10.1029/JA090iA02p01755`.

Bagenal, F., Sullivan, J.D., 1981. Direct plasma measurements in the Io torus and inner magnetosphere of Jupiter. J. Geophys. Res. 86, 8447–8466. doi:`10.1029/JA086iA10p08447`.

Bagenal, F., Wilson, R.J., Siler, S., Paterson, W.R., Kurth, W.S., 2016. Survey of Galileo plasma observations in Jupiter's plasma sheet. Journal of Geophysical Research (Planets) 121, 871–894. doi:`10.1002/2016JE005009`.

Caudal, G., 1986. A self-consistent model of Jupiter's magnetodisc including the effects of centrifugal force and pressure. J. Geophys. Res. 91, 4201–4222. doi:`10.1029/JA091iA04p04201`.

Chané, E., Saur, J., Poedts, S., 2013. Modeling Jupiter's magnetosphere: Influence of the internal sources. Journal of Geophysical Research (Space Physics) 118, 2157–2172. doi:`10.1002/jgra.50258`.

Connerney, J.E.P., Acuna, M.H., Ness, N.F., 1981a. Modeling the Jovian current sheet and inner magnetosphere. J. Geophys. Res. 86, 8370–8384. doi:`10.1029/JA086iA10p08370`.

Connerney, J.E.P., Acuna, M.H., Ness, N.F., 1981b. Saturn's ring current and inner magnetosphere. Nature 292, 724–726. doi:`10.1038/292724a0`.

Connerney, J.E.P., Acuna, M.H., Ness, N.F., 1982. Voyager 1 assessment of Jupiter's planetary magnetic field. J. Geophys. Res. 87, 3623–3623. doi:`10.1029/JA087iA05p03623`.

Connerney, J.E.P., Acuna, M.H., Ness, N.F., 1983. Currents in Saturn's Magnetosphere. J. Geophys. Res. 88, 8779–8790. doi:`10.1029/JA088iA11p08779`.

Connerney, J.E.P., Timmins, S., Herceg, M., Joergensen, J.L., 2020. A Jovian Magnetodisc Model for the Juno Era. Journal of Geophysical Research (Space Physics) 125, e28138. doi:`10.1029/2020JA028138`.

Cowley, S.W.H., Bunce, E.J., 2001. Origin of the main auroral oval in Jupiter's coupled magnetosphere-ionosphere system. Planetary and Space Science 49, 1067–1088. doi:`10.1016/S0032-0633(00)00167-7`.

Cummings, W., Dessler, A., Hill, T., 1980. Latitudinal oscillations of plasma within the io torus. Journal of Geophysical Research: Space Physics 85, 2108–2114. URL: `https://agupubs.onlinelibrary.wiley.com/doi/abs/10.1029/JA085iA05p02108`, doi:`https://doi.org/10.1029/JA085iA05p02108`, `arXiv:https://agupubs.onlinelibrary.wiley.com/doi/pdf/10.1029/JA085iA05p02108`.

Delamere, P.A., Bagenal, F., 2010. Solar wind interaction with Jupiter's magnetosphere. Journal of Geophysical Research (Space Physics) 115, A10201. doi:`10.1029/2010JA015347`.

Dougherty, L.P., Bodisch, K.M., Bagenal, F., 2017. Survey of Voyager plasma science ions at Jupiter: 2. Heavy ions. Journal of Geophysical Research (Space Physics) 122, 8257–8276. doi:`10.1002/2017JA024053`.

Ferraro, V.C.A., 1937. The non-uniform rotation of the Sun and its magnetic field. MNRAS 97, 458. doi:`10.1093/mnras/97.6.458`.

Frank, L.A., Paterson, W.R., Khurana, K.K., 2002. Observations of thermal plasmas in Jupiter's magnetotail. Journal of Geophysical Research (Space Physics) 107, 1003. doi:`10.1029/2001JA000077`.

Gledhill, J.A., 1967. Magnetosphere of Jupiter. Nature 214, 155–156. doi:`10.1038/214155a0`.

Hill, T.W., 1979. Inertial limit on corotation. J. Geophys. Res. 84, 6554–6558. doi:`10.1029/JA084iA11p06554`.

Hill, T.W., 1980. Corotation Lag in Jupiter's Magnetosphere: Comparison of Observation and Theory. Science 207, 301–302. doi:`10.1126/science.207.4428.301`.

Hill, T.W., Dessler, A.J., Michel, F.C., 1974. Configuration of the Jovian magnetosphere. Geophys. Res. Lett. 1, 3–6. doi:`10.1029/GL001i001p00003`.

Hill, T.W., Michel, F.C., 1976. Heavy ions from the Galilean satellites and the centrifugal distortion of the Jovian magnetosphere. J. Geophys. Res. 81, 4561. doi:`10.1029/JA081i025p04561`.

Huang, T.S., Hill, T.W., 1989. Corotation lag of the Jovian atmosphere, ionosphere, and magnetosphere. J. Geophys. Res. 94, 3761–3765. doi:`10.1029/JA094iA04p03761`.

Huscher, E., Bagenal, F., Wilson, R.J., Allegrini, F., Ebert, R.W., Valek, P.W., Szalay, J.R., McComas, D.J., Connerney, J.E.P., Bolton, S., Levin, S.M., 2021. Survey of Juno Observations in Jupiter's Plasma Disk: Density. Journal of Geophysical Research (Space Physics) 126, e29446. doi:`10.1029/2021JA029446`.

Khurana, K.K., 2001. Influence of solar wind on Jupiter's magnetosphere deduced from currents in the equatorial plane. J. Geophys. Res. 106, 25999–26016. doi:`10.1029/2000JA000352`.

Khurana, K.K., Kivelson, M.G., Vasyliunas, V.M., Krupp, N., Woch, J., Lagg, A., Mauk, B.H., Kurth, W.S., 2004. The configuration of Jupiter's magnetosphere. volume 1. pp. 593–616.

Kivelson, M.G., Khurana, K.K., Russell, C.T., Walker, R.J., 1997a. Intermittent short-duration magnetic field anomalies in the Io torus: Evidence for plasma interchange? Geophys. Res. Lett. 24, 2127–2130. doi:`10.1029/97GL02202`.

Kivelson, M.G., Khurana, K.K., Russell, C.T., Walker, R.J., Coleman, P.J., Coroniti, F.V., Green, J., Joy, S., McPherron, R.L., Polanskey, C., Southwood, D.J., Bennett, L., Warnecke, J., Huddleston, D.E., 1997b. Galileo at Jupiter: changing states of the magnetosphere and first looks at IO and ganymede. Advances in Space Research 20, 193–204. doi:`10.1016/S0273-1177(97)00533-4`.

Krimigis, S.M., Carbary, J.F., Keath, E.P., Bostrom, C.O., Axford, W.I., Gloeckler, G., Lanzerotti, L.J., Armstrong, T.P., 1981. Characteristic of hot plasma in the Jovian magnetosphere: Results from the Voyager spacecraft. J. Geophys. Res. 86, 8227–8257. doi:`10.1029/JA086iA10p08227`.

Lorch, C.T.S., Ray, L.C., Arridge, C.S., Khurana, K.K., Martin, C.J., Bader, A., 2020. Local Time Asymmetries in Jupiter's Magnetodisc Currents. Journal of Geophysical Research (Space Physics) 125, e27455. doi:`10.1029/2019JA027455`.

Mauk, B.H., Gary, S.A., Kane, M., Keath, E.P., Krimigis, S.M., Armstrong, T.P., 1996. Hot plasma parameters of Jupiter's inner magnetosphere. J. Geophys. Res. 101, 7685–7696. doi:`10.1029/96JA00006`.

Mauk, B.H., Mitchell, D.G., McEntire, R.W., Paranicas, C.P., Roelof, E.C., Williams, D.J., Krimigis, S.M., Lagg, A., 2004. Energetic ion characteristics and neutral gas interactions in Jupiter's magnetosphere. Journal of Geophysical Research (Space Physics) 109, A09S12. doi:`10.1029/2003JA010270`.

Nichols, J., Cowley, S., 2004. Magnetosphere-ionosphere coupling currents in Jupiter's middle magnetosphere: effect of precipitation-induced enhancement of the ionospheric Pedersen conductivity. Annales Geophysicae 22, 1799–1827. doi:`10.5194/angeo-22-1799-2004`.

Nichols, J.D., 2011. Magnetosphere-ionosphere coupling at Jupiter-like exoplanets with internal plasma sources: implications for detectability of auroral radio emissions. MNRAS 414, 2125–2138. doi:`10.1111/j.1365-2966.2011.18528.x`, `arXiv:1102.2737`.

Nichols, J.D., Achilleos, N., Cowley, S.W.H., 2015. A model of force balance in Jupiter's magnetodisc including hot plasma pressure anisotropy. Journal of Geophysical Research (Space Physics) 120, 10,185–10,206. doi:`10.1002/2015JA021807`.

Nichols, J.D., Allegrini, F., Bagenal, F., Bunce, E.J., Cowley, S.W.H., Ebert, R.W., Grodent, D., Huscher, E., Kamran, A., Kurth, W.S., Wilson, R.J., Yao, Z., 2020. An enhancement of jupiter's main auroral emission and magnetospheric currents. Journal of Geophysical Research: Space Physics 125, e2020JA027904. URL: `https://agupubs.onlinelibrary.wiley.com/doi/abs/10.1029/2020JA027904`, doi:`https://doi.org/10.1029/2020JA027904`, `arXiv:https://agupubs.onlinelibrary.wiley.com/doi/pdf/10.1029/2020JA027904`. e2020JA027904 10.1029/2020JA027904.

Nichols, J.D., Cowley, S.W.H., 2003. Magnetosphere-ionosphere coupling currents in JupiterÂ's middle magnetosphere: dependence on the effective ionospheric Pedersen conductivity and iogenic plasma mass outflow rate. Annales Geophysicae 21, 1419–1441. doi:`10.5194/angeo-21-1419-2003`.

Phipps, P., Bagenal, F., 2021. Centrifugal equator in jupiter's plasma sheet. Journal of Geophysical Research: Space Physics 126, e2020JA028713. URL: `https://agupubs.onlinelibrary.wiley.com/doi/abs/10.1029/2020JA028713`, doi:`https://doi.org/10.1029/2020JA028713`, `arXiv:https://agupubs.onlinelibrary.wiley.com/doi/pdf/10.1029/2020JA028713`. e2020JA028713 2020JA028713.

Pontius, D.H., 1997. Radial mass transport and rotational dynamics. J. Geophys. Res. 102, 7137–7150. doi:`10.1029/97JA00289`.

Simpson, J.A., Hamilton, D., Lentz, G., McKibben, R.B., Mogro-Campero, A., Perkins, M., Pyle, K.R., Tuzzolino, A.J., O'Gallagher, J.J., 1974. Protons and Electrons in Jupiter's Magnetic Field: Results from the University of Chicago Experiment on Pioneer 10. Science 183, 306–309. doi:`10.1126/science.183.4122.306`.

Siscoe, G.L., 1978. Jovian plasmaspheres. J. Geophys. Res. 83, 2118–2126. doi:`10.1029/JA083iA05p02118`.

Smith, E.J., Davis, L., J., Jones, D.E., Coleman, P. J., J., Colburn, D.S., Dyal, P., Sonett, C.P., 1975. Jupiter's Magnetic Field, Magnetosphere, and Interaction with the Solar Wind: Pioneer 11. Science 188, 451–455. doi:`10.1126/science.188.4187.451`.

Stern, D.P., 1970. Euler Potentials. American Journal of Physics 38, 494–501. doi:`10.1119/1.1976373`.

Thorne, R.M., Armstrong, T.P., Stone, S., Williams, D.J., McEntire, R.W., Bolton, S.J., Gurnett, D.A., Kivelson, M.G., 1997. Galileo evidence for rapid interchange transport in the Io torus. Geophys. Res. Lett. 24, 2131–2134. doi:`10.1029/97GL01788`.